The non–muscle actinopathy–associated mutation E334Q in cytoskeletal γ–actin perturbs interaction of actin filaments with myosin and ADF/cofilin family proteins

Johannes N. Greve[1], Anja Marquardt[1], Robin Heiringhoff[1], Theresia Reindl[1§], Claudia Thiel[1], Nataliya Di Donato[2], Manuel H. Taft[1], Dietmar J. Manstein[1,3,4,*]

1 Institute for Biophysical Chemistry, Hannover Medical School, Fritz–Hartmann–Centre for Medical Research, 30625 Hannover, Germany

2 Department of Human Genetics, Hannover Medical School, 30625 Hannover, Germany

3 Division for Structural Biochemistry, Hannover Medical School, 30625 Hannover, Germany

4 RESiST, Cluster of Excellence 2155, Hannover Medical School, 30625 Hannover, Germany

[§]Present address: Department of Microbiology and Immunology, Stanford University School of Medicine, 279 Campus Drive West, Stanford CA 94305, USA

*Corresponding author

Abstract

Various heterozygous cytoskeletal γ–actin mutations have been shown to cause Baraitser–Winter cerebrofrontofacial syndrome, non–syndromic hearing loss, or isolated eye coloboma. Here, we report the biochemical characterization of human cytoskeletal γ–actin carrying mutation E334Q, a mutation that leads to a hitherto unspecified non–muscle actinopathy. Following expression, purification, and removal of linker and thymosin β4 tag sequences, the p.E334Q monomers show normal integration into linear and branched actin filaments. The mutation does not affect thermal stability, actin filament nucleation, elongation and turnover. Model building and normal mode analysis predict significant differences in the interaction of p.E334Q–filaments with myosin motors and members of the ADF/cofilin family of actin–binding proteins. Assays probing the interactions of p.E334Q–filaments with human class 2 and class 5 myosin motor constructs show significant reductions in sliding velocity and actin–affinity. E334Q differentially affects cofilin-mediated actin dynamics by increasing the rate of cofilin-mediated *de novo* nucleation of actin filaments and decreasing the efficiency of cofilin-mediated filament severing. Thus, it is likely that p.E334Q-mediated changes in myosin motor activity, as well as filament turnover contribute to the observed disease phenotype.

Introduction

Cytoskeletal β– and γ–actin are the basic building blocks of the actin cytoskeleton in human non–muscle cells. The spatio–temporal regulation of these two actin isoforms, mediated by distinct actin–binding proteins (ABPs), drives the establishment and maintenance of specialized cytoskeletal compartments that are defined by their network architecture and the presence of specific filamentous actin–associated proteins (Pollard, 2016; Plastino & Blanchoin, 2019). The regulated ATP–dependent turnover of these actin networks as well as the coordinated interplay of actin with network–specific ABPs contribute to essential cellular processes like directed migration, adhesion, division and mechanotransduction (Ponti *et al*, 2004; Abercrombie *et al*, 1970, 1971; Ridley *et al*, 2003; Pollard *et al*, 2002; Lauffenburger & Horwitz, 1996).

β– and γ–actin differ by only four amino acids in the N–terminal region of the molecule but show isoform–specific spatial organization in studies performed with monoclonal antibodies. In motile and stationary cells, β–actin is found in contractile stress fibers and the cell periphery (Dugina *et al*, 2009; Latham *et al*, 2013; Dugina *et al*, 2015). In contrast, γ–actin localization is less static. During cell movement, γ–actin is recruited to the leading edge of the cell, resulting in an enrichment of the isoform in the lamellipodium together with β–actin (Dugina *et al*, 2009). In non–moving cell states, γ–actin is co–localized with β–actin in stress fibers (Dugina *et al*, 2009). In order to reconcile the highly similar protein sequences with the varying localization, several hypotheses on isoform regulation were put forward. These include the preferential interaction of ABPs with a particular isoform depending on the minor differences in the protein sequence, post–translational modifications as a means of isoform–specific regulation, and differences in the translation speed of *ACTB* and *ACTG1,* the genes encoding cytoskeletal β–actin and γ–actin (Zhang *et al*, 2010; Vedula *et al*, 2017; Pavlyk *et al*, 2018; Müller *et al*, 2013).

Diseases associated with heterozygous pathogenic variants in *ACTB* and *ACTG1* are typically referred to as non–muscle actinopathies. These include a spectrum of rare syndromes that manifest themselves as more or less pronounced developmental disorders in patients (Verloes *et al*, 2015; Di Donato *et al*, 2014; Latham *et al*, 2018; Rivière *et al*, 2012; Baraitser & Winter, 1988; Cuvertino *et al*, 2017). Baraitser–Winter–Cerebrontofacial–Syndrome (BWCFF, (Baraitser & Winter, 1988)) is a condition that affects the development of multiple organs, but particularly results in facial anomalies and brain malformations. BWCFF occurs due to various missense mutations in *ACTB* or *ACTG1* (Verloes *et al*, 2015; Di Donato *et al*, 2014; Rivière *et al*, 2012; Di Donato *et al*, 2016). BWCFF–patients show a recognizable facial gestalt, with variants in *ACTB* generally resulting in a stronger facial phenotype than mutations in *ACTG1* (Di Donato *et al*, 2014). BWCFF–patients regularly suffer from cortical malformations that lead to severe developmental and mental impairments. In addition, symptoms such as hearing loss, dystonia, hypotonia and polydactyly occur with increased frequency (Di Donato *et al*, 2014; Rivière *et al*, 2012). Variants in *ACTB* alone are responsible for two other well–defined syndromes. *ACTB*–associated pleiotropic malformation syndrome and *ACTB*–associated syndromic thrombocytopenia can be caused by single–point missense mutations, truncating mutations, frameshift mutations or deletion (Latham *et al*, 2018; Cuvertino *et al*, 2017). These *ACTB*–associated syndromes differ from BWCFF in that they cause only mild craniofacial malformations and developmental disorders (Cuvertino *et al*, 2017; Latham *et al*, 2018). Selected single–point missense mutations in *ACTG1* lead to a non–syndromic form of hearing loss (Rendtorff *et al*, 2006; van Wijk *et al*, 2003; Yuan *et al*, 2016).

How exactly mutations in the ubiquitously produced actin isoforms of the cytoskeleton lead to various syndromes and mutation-specific symptoms remains unclear. Currently, four main disease mechanisms are under discussion (Greve *et al*, 2022; Costa *et al*, 2004). First, mutations in the actin isoform can lead to functional haploinsufficiency, where the produced molecule is either intrinsically unstable and therefore degraded by the proteasome or unable to associate with other actin molecules and thus unable to partake in the necessary steps involved in the dynamic remodeling of the actin cytoskeleton. This results in a reduced amount of "active" actin molecules, which cannot fully be compensated for by the remaining allele (Vang *et al*, 2005). Second, the mutant protein is produced in normal quantities and integrated into filaments but interferes with actin filament turnover (Costa *et al*, 2004). Third, the mutation perturbs interactions with actin binding proteins, either by direct or allosteric disturbance of actin–actin or actin–ABP interaction interfaces (Greve *et al*, 2022; Hundt *et al*, 2014; Bryan *et al*, 2006; Müller *et al*, 2012). Fourth, the mutant protein shows an increased propensity for forming toxic rod–like oligomeric structures, which can potentially harm the cell (Ilkovski *et al*, 2004; Schröder *et al*, 2004).

Therefore, one of the significant challenges is elucidating the relationship between the disturbed molecular mechanisms of the cell's actin dynamics and disease patterns observed in patients. In order to achieve this, it is necessary to resolve the structure–function relationship of the various actin mutations at the molecular level.

Here, we report the biochemical characterization of p.E334Q, a cytoskeletal γ–actin variant, which causes a syndromic form of non–muscle actinopathy. Features associated with the production of p.E334Q include mild facial anomalies and an abnormal gyral pattern of the cerebral cortex (Di Donato *et al*, 2016). At four years (age of diagnosis), a patient carrying this mutation showed developmental delay and severe muscle hypotonia (Di Donato *et al*, 2016). Although the patient was initially reported within the *ACTG1*–associated BWCFF cohort, careful reassessment of the phenotype revealed that the clinical phenotype cannot be classified as BWCFF and is therefore assigned as an unclassified NMA.

Structural analysis of the disease–causing mutation shows that residue E334 is located in the hinge region of the actin molecule, which connects the two subdomain pairs of the protein. The region's flexibility and ability to act as a pivot point are essential for the subdomain rearrangement when actin monomers polymerize into filaments (**Figure 1A**). Furthermore, E334 is part of a contact region on the F–actin surface that interacts with the so-called cardiomyopathy–loop in the motor domain of cytoskeletal myosin isoforms and contributes to the formation of the actin–cofilin complex (**Figure 3**).

Here, we present experimental evidence for the impact of changes involving residue E334 with respect to productive interactions with cytoskeletal myosin isoforms, actin polymerization dynamics, and the formation of stable actin-cofilin complexes. We show that mutation E334Q does not adversely affect protein folding. The thermal stability of p.E334Q resembles that of the wild–type protein, both as a monomer and following integration into filaments. The mutant protein efficiently copolymerizes with wildtype (WT) monomers and integrates into linear and branched filament networks. In contrast, the interaction of mutant filaments with non-muscle myosin-2A/C and myosin-5A is strongly impaired, as shown by *in vitro* motility experiments and solution kinetics. Furthermore, p.E334Q filaments are less susceptible to cofilin–mediated disassembly, while monomers are more susceptible to cofilin–mediated nucleation.

Results

Production of cytoskeletal γ–actin and its variant p.E334Q

We produced untagged cytoskeletal γ–actin and its variant p.E334Q in insect cells, free of contaminating endogenous *S. frugiperda* actin, using a method that was originally designed for the production of toxic actin mutants in *Dictyostelium discoideum* and later adapted for use with the baculovirus/Sf9 insect cell expression system (Noguchi *et al*, 2007; Lu *et al*, 2015). The monomeric actin constructs were initially produced fused to the actin-monomer sequestering protein thymosin-β4. Purification of the fusion protein by immobilized metal affinity chromatography, followed by chymotrypsin–mediated cleavage of C–terminal linker and tag sequences, results in homogeneous protein without non–native residues and native N-terminal processing, which includes cleavage of the initial methionine and acetylation of the following glutamate. The method worked equally well for both WT and mutant actin. Starting with 2×10^9 cells, typical yields ranged from 5–7 mg of purified protein for cytoskeletal γ–actin and p.E334Q (N=3 for WT and N=4 for p.E334Q) (**Figure 1– figure supplement 1**).

Impact of mutation E334Q on protein folding and thermal stability

Mutation–induced misfolding of actin has been identified as one of the main causes for the development of actinopathies (Bryan *et al*, 2006; Vang *et al*, 2005). Residue E334 is located in the hinge region, formed by residues 137–145 and 333–338 (**Figure 1A**), which is strongly involved in the structural reorganization of the monomer upon incorporation into a growing filament (Dominguez & Holmes, 2011). Previous studies have shown that an intact hinge region is crucial for the interactions with the eukaryotic chaperonin CCT/TriC and myosin (Noguchi *et al*, 2012; McCormack *et al*, 2001b, 2001a). We first performed a DNase–I inhibition assay to analyze the effect of mutation E334Q on the folding of the protein. Previous studies have shown that the activity of DNase–I is only effectively inhibited by correctly folded actin (Schüler *et al*, 2000). We observed a 10% increase in the apparent IC_{50}–value of p.E334Q (25.7± 0.6 nM) compared to the WT protein (22.7± 0.7 nM) (**Figure 1B)**. This is in good agreement with CD–spectroscopy results showing nearly identical secondary structure compositions for WT and mutant proteins (**Figure 1 – figure supplement 2)**. Thermal denaturation temperatures (T_M) analyzed by differential scanning fluorimetry (DSF) gave values of 56.77 ± 0.24°C and 56.19 ± 0.30°C for monomeric WT actin and p.E334Q. The values obtained for WT and E334Q filaments were 65.00 ± 0.76°C and 64.83 ± 0.25°C, respectively (**Figure 1C, Table 1)**. Overall, these results show that the mutant actin is correctly folded and has comparable stability to the WT protein.

As the hinge region is in close proximity to the nucleotide–binding cleft, we examined a potential effect of the mutation on the interaction with nucleotides and the turnover of ATP. Initial tests gave near identical rates of 0.00089 ± 0.00005 s^{-1} and 0.00088 ± 0.00004 s^{-1} for the steady–state turnover of ATP by filaments formed from cytoskeletal γ–actin or the p.E334Q variant (**Table 1**). Next, we determined the nucleotide dissociation rates k_{-T} and k_{-D} by monitoring the decrease in fluorescence amplitude associated with the displacement of ε–ATP or ε–ADP after rapid mixing with a large excess of unlabeled ATP. With p.E334Q-actin, we observed rates of k_{-T}=0.0972 ± 0.0019 s^{-1} and k_{-D}=0.3199 ± 0.0027 s^{-1}. These rates are about 2-fold and 1.5-fold faster than those observed in experiments performed with WT monomers (k_{-T}=0.0473 ± 0.0013 s^{-1}, k_{-D}= 0.2155 ± 0.0017 s^{-1} (**Figure 1D, Table 1**). The observed nucleotide dissociation rates for human cytoskeletal γ–actin are in good agreement with values

163 obtained for a mixture of pyrene-labeled cytoskeletal γ–actin (15%) and β–actin (85%) purified from
164 human platelets in experiments performed at the same ionic strength (De La Cruz & Sept, 2010).

165

166 p.E334Q shows normal polymerization behavior and is efficiently integrated into 167 linear and branched actin structures

168 The regulated assembly and disassembly of filamentous actin drive various cellular processes, including
169 directed cell migration, adhesion and endocytosis. A slight conformational change of the actin
170 monomer accompanies the integration of a monomeric actin molecule into a growing filament. A small
171 change in the hinge region leading to a 12° to 13° rotation of the inner subdomain pair relative to the
172 outer subdomain pair results in a flatter actin molecule within the filament compared to the free actin
173 monomer (Dominguez & Holmes, 2011; Oda *et al*, 2009). Mutations in the hinge region can thus
174 potentially affect filament assembly by impairing the required structural reorganization of the
175 monomer, as it attaches to the growing filament end. TIRF microscopy–based tracking of the
176 polymerization of monomeric Atto–655–labeled WT or mutant actin *in vitro* revealed a small but
177 significant reduction in the elongation rate from 12.6 ± 0.3 nm s^{-1} for WT to 11.1 ± 0.3 nm s^{-1} for mutant
178 filaments (**Figure 2A, B**). To detect any differences in nucleation efficiency, we determined the time-
179 dependent increase in the number of filaments (**Figure 2C**). Aside from short-term fluctuations, the
180 linear increase in the number of filaments recorded for WT (0.039 ± 0.002 s^{-1}) and p.E334Q (0.041 ±
181 0.004 s^{-1}) was similar over the full 1000 s duration of the experiment. Overall, p.E334Q shows only a
182 mild polymerization defect.

183 Since actin polymerization *in vivo* is tightly regulated in a spatio–temporal manner by different ABPs,
184 we analyzed the interaction of p.E334Q with one of the key–regulators of actin polymerization, the
185 Arp2/3 complex (Goley & Welch, 2006). The Arp2/3 complex promotes the nucleation of new actin
186 filaments from the sides of existing filaments and caps their pointed ends. Thereby, it promotes the
187 formation of branched actin networks and contributes to essential processes that depend on the
188 dynamic remodeling of the actin cytoskeleton, such as cell migration, endocytosis, and organelle
189 positioning (Nicholson-Dykstra *et al*, 2005; Mullins *et al*, 1998; Blanchoin *et al*, 2000; Loisel *et al*, 1999).
190 The ability of p.E334Q to form branched actin networks was probed in TIRF microscopy–based
191 experiments in the presence of increasing concentrations of VCA–activated human Arp2/3 complex
192 (**Figure 2D**). At the lowest Arp2/3 concentration used (0.01 nM), we observed the appearance of the
193 first branches after approximately 250 s. In the presence of 0.1 nM and 0.2 nM of the VCA-activated
194 Arp2/3 complex, mutant and WT actin continued forming branched networks with comparable branch
195 formation and branch elongation rates. Similar results were obtained with WT actin, mutant actin or
196 with 1:1 mixtures of WT and mutant actin, when we analyzed the effect of adding increasing
197 concentrations of VCA–activated human Arp2/3 in pyrene–actin based bulk–polymerization assays
198 (**Figure 2E, F**). The results are summarized in **Table 1**.

199

200 Impact of E334Q mutation on interactions with ADF/cofilin family proteins

201 Homology models of the complexes formed by human cofilin–1 with filamentous cytoskeletal γ–actin
202 and p.E334Q were generated to evaluate the functional impact of mutation E334Q. Cofilin-1 binds to
203 actin filaments by making simultaneous contact with two adjacent monomers. Actin residue E334 is
204 located halfway between two adjacent cofilin molecules, but only makes direct contact with residue

205 L111 of the cofilin–1 molecule on the pointed end side (**Figure 3A**). Cofilin–1 residue L111 is located in
206 an α-helix (L111-L128) that is essential for actin–binding (Pope *et al*, 2000). Mutation E334Q maintains
207 the van der Waals interaction with L111, but reduces the electrostatic attraction between the
208 interacting surfaces, with likely effects on the stability and allosteric coupling of the complex (**Figure**
209 **3B, C**).

210 To evaluate the impact of mutation E334Q on the elastic properties of F–actin in the presence and
211 absence of cofilin–1 binding, we performed normal mode analysis using bare, partially decorated and
212 fully decorated filaments ((**Figure 3, Figure 3 – figure supplement 1A)**. Since residue E334 is located
213 on the outer surface of the actin filament, the mutation produces no significant change in the normal
214 mode frequencies of bare filaments. Similarly, fully decorated filaments show only minor differences.
215 Substantial changes in the low-frequency modes associated with global conformational changes were
216 observed when comparing the partially cofilin-decorated filaments of WT and mutant filaments, where
217 the bare and cofilin–decorated regions move as rigid bodies and the interface between the two regions
218 acts as a hinge (modes 7, 8) or fulcrum (mode 9) (**Figure 3 – figure supplement 1B)**.

219 To test the validity of our modeling results, we performed biochemical and functional assays probing
220 the interactions of human cofilin–1 with monomeric and filamentous cytoskeletal γ–actin and p.E334Q.
221 The effect of cofilin–1 on filament assembly was assessed by TIRF microscopy experiments. The
222 polymerization of 1 µM actin was induced in the presence of 0, 50 or 100 nM cofilin–1. Following an
223 initial lag phase of 200 to 300 seconds, the filament formation rate increased with the cofilin–1
224 concentration (**Figure 4**). In experiments with p.E334Q-actin, *de novo* filament nucleation proceeded
225 faster (**Figure 4A, B**). Movies showing filament formation by *de novo* nucleation in the presence of
226 cofilin-1 are available in **Figure 4 – video supplement 1–6.**

227 Next, we investigated the effect of cofilin–1 on the disassembly of preformed cytoskeletal γ–actin and
228 p.E334Q filaments. The effect of cofilin–1 on existing WT and mutant filaments was initially tested by
229 performing pyrene–based dilution–induced disassembly experiments with actin filaments polymerized
230 for 16 hours and containing predominately ADP–actin. Cofilin–1 has previously been shown to increase
231 the bulk–disassembly rate of actin in this experimental setup (Breitsprecher *et al*, 2011; Greve *et al*,
232 2022). In the absence of cofilin, the changes in pyrene–fluorescence are best described by single
233 exponential functions with k_{obs} values of 0.0022 ± 0.0002 $s^{-1}$and 0.0029 ± 0.0003 s^{-1} for WT and p.E334Q
234 filaments, respectively (**Figure 5A, Figure 5– figure supplement 1)**. The addition of cofilin–1 increased
235 the observed rate of the dilution–induced disassembly in a concentration–dependent manner for both
236 mutant and WT filaments. At the highest cofilin–1 concentration used (40 nM), the change in pyrene–
237 fluorescence with p.E334Q filaments is still best described by a single exponential function with a k_{obs}
238 value of 0.0059 ± 0.0008 s^{-1}. In contrast, the change for WT filaments is best-fitted to a bi-exponential
239 function. Here, the k_{obs} values for the fast and slow phases are 0.0163 ± 0.0028 s^{-1} and 0.0002 ± 0.00003
240 s^{-1}, respectively (**Figure 5A, Figure 5 – figure supplement 1)**. Additional experiments with
241 heterofilaments showed milder but significant differences (**Table 1**). The observed rate constant values
242 were linearly dependent on the concentration of cofilin–1 in the range 0–40 nM, with the slopes
243 corresponding to the apparent second–order rate constant (k_C) for the cofilin-1 induced
244 depolymerization of F–actin. In experiments performed with p.E334Q filaments, the value obtained for
245 k_C was 4.2-fold lower ($0.81 \times 10^{-4} \pm 0.08 \times 10^{-4}$ nM^{-1} s^{-1}) compared to experiments with WT filaments
246 ($3.42 \times 10^{-4} \pm 0.22 \times 10^{-4}$ nM^{-1} s^{-1}). When heterofilaments were used, the effect of the mutation was
247 reduced to a 2.2-fold difference compared to WT filaments ($1.54 \times 10^{-4} \pm 0.11 \times 10^{-4}$ nM^{-1} s^{-1}).

248 The pyrene-based bulk experiments show an evident change in the p.E334Q–cofilin interaction.
249 However, they cannot distinguish between cofilin–1 binding defects and a disassembly efficiency
250 change. To analyze the perturbed interaction of p.E334Q with cofilin–1 in more detail, we first
251 performed high-speed co–sedimentation assays with constant concentrations of F–actin (5 µM) and
252 increasing concentrations of cofilin-1 (0.0625 – 20 µM) at pH 6.5 and pH 7.8. Cofilin-1 binds faster but
253 severs filaments less efficiently under slightly acidic pH conditions, whereas a weakly basic
254 environment favors cofilin–mediated severing (Wioland *et al*, 2019). We first performed experiments
255 at pH 6.5. This endpoint experiment showed that cofilin–1 binds to and disassembles p.E334Q and WT
256 filaments (**Figure 5B, C)**. Most pellet fractions from the experiments conducted with WT filaments were
257 found to contain less cofilin-1, as higher disassembly efficiency results in more cofilin–1 being bound
258 to actin monomers and retained in the supernatant fraction. We repeated the experiment at pH 7.8
259 with an equimolar and a 2–fold excess of cofilin, (**Figure 5B, C**). In experiments with equimolar cofilin–
260 1, we found significantly less WT actin in the pellet fraction than at pH 6.5, consistent with a higher
261 disassembly–efficiency at pH 7.8. The shift to pH 7.8 did not have the same enhancing effect on the
262 disassembly of p.E334Q filaments, as indicated by an increase of p.E334Q actin in the pellet fraction.
263 The endpoint measurements show that cofilin–1 binds to p.E334Q filaments but severs them less
264 efficiently. Next, we performed fluorescence quench experiments with pyrene-labeled WT and
265 p.E334Q filaments, as it was previously shown that cofilin-1 efficiently quenches the fluorescence of
266 pyrene-labeled actin filaments (Blanchoin & Pollard, 1999; De La Cruz, 2005). We determined the
267 change in fluorescence amplitude when 2 µM pyrene-labeled p.E334Q or WT filaments were mixed
268 with increasing concentrations of cofilin-1. Fitting a quadratic equation to the obtained experimental
269 values gave only slightly different dissociation equilibrium constants of $K_{D,\ p.E334Q}$ = 1.83 ± 0.13 µM and
270 $K_{D,\ WT}$ = 1.61 ± 0.07 µM (**Figure 5D**). These K_D values are in the range of values previously determined
271 for muscle α-actin filaments (Blanchoin & Pollard, 1999; De La Cruz, 2005), actin filaments from
272 *Acanthamoeba castellanii* (Blanchoin & Pollard, 1999) and filaments containing a mixture of human γ–
273 and β–actin (De La Cruz, 2005) using the same method.

274 To better understand the underlying changes leading to the differences in cofilin–mediated filament
275 disassembly efficiency, we performed two–color TIRF microscopy experiments using Atto–655 labeled
276 WT or mutant filaments and eGFP–cofilin–1. This setup allows us to observe the binding of eGFP–
277 cofilin–1 to individual filaments and the resulting disassembly of the filaments in real–time. eGFP–
278 cofilin–1 was shown to bind to actin filaments and disassemble actin as efficiently as WT cofilin–1
279 (Wioland *et al*, 2019, 2017; Breitsprecher *et al*, 2011). Immediately after mixing 300 nM "aged" actin
280 filaments, capped at their barbed end by human capping protein (CP), with 100 nM eGFP–cofilin–1,
281 the reaction mixture was flushed into a flow–chamber and imaging was started. The delay between
282 mixing and the start of imaging was approximately 15 seconds for each sample. At the end of the
283 experimental dead time, almost twice as many cofilin clusters had formed in the field of view on WT
284 filaments (151 ± 29) as on p.E334Q filaments (82 ± 6) (**Figure 6A**), the number of both WT and mutant
285 actin filaments had doubled from initially about 95 to about 200 filaments (**Figure 6B**), and the Atto–
286 655 fluorescence of the WT filaments had decreased to 30% of the starting value, whereas the Atto–
287 655 fluorescence of p.E334Q filaments remained unchanged (**Figure 6C**). During the following 500 s,
288 total eGFP-cofilin-1 fluorescence increased linearly, with the rate of increase being approximately
289 twice as fast for WT as for p.E334Q filaments (**Figure 6D**). While the total eGFP-cofilin-1 fluorescence
290 in the presence of p.E334Q filaments continued to increase linearly over the next 1000 seconds, the
291 signal for WT filaments began to saturate and reached a plateau value (**Figure 6D**). The number of
292 cofilin clusters on WT filaments decreased steadily during the observation period of 1500 s. In contrast,

293 their number increased in the presence of p.E334Q filaments, reaching a maximum after 500 s,
294 followed by a plateau of 400 s and a subsequent slow decrease (**Figure 6A**). The changes in the number
295 of actin filaments showed similar time dependencies, a steady decrease for WT filaments and an initial
296 increase for p.E334Q filaments followed immediately by a linear decrease without an intervening
297 plateau phase (**Figure 6B**). For WT and p.E334Q filaments, the size of eGFP–cofilin–1 clusters on the
298 steadily shrinking filaments expanded continuously until either severing occurred or the actin filament
299 was fully decorated. No severing events were observed with fully decorated filaments.

300

301 Impact of E334Q mutation on interactions with myosin family proteins

302 The precise nature of the six actin-binding elements in the myosin motor domain varies considerably
303 among myosin isoforms (Sellers, 2000; Cope *et al*, 1996). The associated sequences have conserved
304 hydrophobic and electrostatic properties, variations of which contribute to the tuning of kinetic and
305 functional properties. Actin residue E334 interacts with a positively charged patch in the
306 cardiomyopathy loop (CM–loop) of the myosin upper 50 kDa domain of NM2C and Myo5A (Pospich *et*
307 *al*, 2021; Von Der Ecken *et al*, 2016). In the case of NM2C, the electrostatic interaction of E334 with
308 K429 in the CM–loop is further stabilized by van der Waals interactions with I420 and V427 (**Figure 7**).
309 A lysine residue corresponding to K429 in NM2C is present in all human myosin–2 and myosin–5
310 isoforms. During force-generating interactions with mutant actin filaments, the weakening of
311 complementary electrostatic interactions in this region of the actomyosin interface is likely to
312 attenuate the binding affinity of class 2 and 5 myosins as well as the coupling between their actin and
313 nucleotide binding sites.

314 Cytoskeletal γ–actin filaments move with an average sliding velocity of 195.3 ± 5.0 nm s^{-1} on lawns of
315 surface immobilized NM2A–HMM molecules (**Figure 8A, B**). For NM2A-HMM densities below about
316 10,000 molecules per μm^2, the average sliding speed for cytoskeletal actin filaments drops steeply
317 (Hundt *et al*, 2016). Filaments formed by p.E334Q actin move 5-fold slower, resulting in an observed
318 average sliding velocity of 39.1 ± 3.2 nm/s. Filaments copolymerized from a 1:1 mixture of WT and
319 p.E334Q actin move with an average sliding velocity of 131.2 ± 10 nm s^{-1} (**Figure 8A, B**). When equal
320 densities of surface-attached WT and mutant filaments were used, we observed that the number of
321 rapid dissociation and association events increased markedly for p.E334Q filaments (**Figure 8 – video**
322 **supplement 7–9)**.

323 Using a NADH-coupled enzymatic assay, we determined the ability of p.E334Q and WT filaments to
324 activate the ATPase of NM2A-HMM over the range of 0-25 µM F-actin (**Figure 8C**). While we observed
325 no significant difference in $K_{app,}$ indicated by the actin concentration at half-maximal activation, in
326 experiments with p.E334Q filaments (2.89 ± 0.49 µM) and WT filaments (3.20 ± 0.74 µM), we observed
327 a 28% slower maximal ATP turnover at saturating actin concentration (k_{cat}) with p.E334Q filaments
328 (0.076 ± 0.005 s^{-1} vs. 0.097 ± 0.002 s^{-1}). To investigate the impact of the mutation on actomyosin–
329 affinity using transient–kinetic approaches, we determined the dissociation rate constants using a
330 single–headed NM2A–2R construct (**Figure 8D**). NM2A–2R is a constitutively active motor–domain
331 construct generated by fusing the motor–domain of NM2A to two spectrin–like repeats serving as a
332 rigid lever arm extension (Anson *et al*, 1996). The construct is ideally suited for the kinetic
333 characterization of the NM2–isoforms (Heissler & Manstein, 2011). The dissociation rate constant k_{-A}
334 is 5.6–fold increased from 0.08 × 10^{-3} s^{-1} to 0.45 × 10^{-3} s^{-1} for NM2A–2R when p.E334Q filaments are
335 used. A similar change from 0.31 × 10^{-3} s^{-1} to 1.70 × 10^{-3} s^{-1} was observed for the analogous NM2C–2R

construct (**Figure 8 – figure supplement 1**). Next, we determined the affinities of NM2A–2R for WT and p.E334Q filaments in the absence of nucleotide (K_A) and the presence of saturating concentrations of ADP (K_{DA}). We performed affinity–titration experiments with pyrene–labeled, phalloidin–stabilized filaments and NM2A–2R (Kurzawa & Geeves, 1996). The values measured under rigor conditions show a 9.9-fold reduced affinity of NM2A–2R for p.E334Q filaments (K_A = 16.9 ± 1.3 nM) compared to WT filaments (K_A = 1.7 ± 0.3 nM) (**Figure 8E**). When the experiment was performed in the presence of saturating concentrations of ADP, we obtained values for K_{DA} of 353.0 ± 20.6 nM in the presence of p.E334Q filaments and 122.6 ± 11.4 nM with WT filaments (**Figure 8F**). The apparent ATP–affinity ($1/K_1$), the maximal dissociation rate of NM2A from F-actin in the presence of ATP (k_{+2}), and the apparent second-order rate constant of ATP binding (K_1k_{+2}) showed no significant differences for complexes formed between NM2A and WT or p.E334Q filaments (**Table 1, Figure 8 – figure supplement 3**).

Next, we investigated the effects of the E334Q mutation on the motile activity of the processive motor Myo5A (**Figure 9**). Since the lysine residue corresponding to K429 in the CM loop of NM2C is also present in all human myosin 5 isoforms, the resulting changes in binding strength and thermodynamic coupling are expected to reduce the motor activity of Myo5A upon interactions with p.E334Q filaments. Structural studies have shown that the interaction between actin residue E334 and the CM-loop in the Myo5A motor domain is maintained from the rigor to the ADP–bound state (Pospich *et al*, 2021). We performed unloaded *in vitro* motility assays to evaluate the effect of the mutation on the interaction with Myo5A–HMM. The rapid transition from weak to strong binding with a slow and rate-limiting ADP release leading to a high working ratio (De La Cruz *et al*, 1999) allows the *in vitro* motility assay to be performed on surfaces with a low motor density. In initial experiments, we found a Myo5A–HMM surface density of 770 molecules μm^{-2} to be optimal for experiments with WT filaments. This much lower optimal motor surface density compared to the NM2A-HMM construct, which requires densities above 10,000 molecules per μm^2, is a manifestation of the processive properties of the Myo5A– HMM construct. Movement was steady and filament breaks were practically non–existent at 770 molecules μm^{-2}, while higher surface densities led to increased filament breaks, resulting in rapid fragmentation. At all Myo5A–HMM surface densities used, the sliding velocity was significantly reduced for p.E334Q compared to WT filaments. In experiments with p.E334Q filaments, a 4-fold higher Myo5A–HMM surface density was required to achieve a similar actin surface decoration and optimal motile activity. Furthermore, filament breaks occurred less frequently, indicating a weaker actomyosin interaction. The number of moving filaments and their sliding velocity decreased sharply below surface densities of 770 molecules μm^{-2} for WT filaments and 3100 molecules μm^{-2} for p.E334Q filaments. Below a surface density of 380 Myo5A–HMM molecules μm^{-2}, no productive attachment events were observed with p.E334Q filaments. Thus, mutation E334Q in cytoskeletal γ–actin leads to an impairment of the interaction of the actin filament with Myo5A, similar to the changes observed with NM2A and NM2C, but with additional manifestations specific to processive motors.

Discussion

At present, the exact pathogenesis of non-muscular actinopathies remains poorly understood. A rigorous molecular characterization of the contribution of disturbances in actin dynamics, contractility and transport processes is necessary to develop an understanding of the diverse disease patterns.

378 In the past, the functional characterization of disease–associated mutations in cytoskeletal γ–actin
379 focused on mutations p.T89I, p.K118N/M, p.E241K, p.T278I, p.P264L, p.P332A, and p.V370A, which all
380 cause non–syndromic hearing loss. Two mutants showed abnormal polymerization behavior, indicated
381 by a reduced polymerization rate (p.V370A) (Bryan *et al*, 2006) or an increased propensity for bundle
382 formation (p.E241K) (Morín *et al*, 2009). The mutants p.K118N/M showed a perturbed interaction with
383 the Arp2/3 complex, reducing branching efficiency (Kruth & Rubenstein, 2012; Jepsen *et al*, 2016). A
384 significantly reduced protein stability was observed for two mutant proteins (p.P264L, p.P332A) (Bryan
385 *et al*, 2006). Perturbed interactions with cofilin were observed for a range of mutations. p.T89I,
386 p.E241K, p.T278I, and p.V370A are characterized by an increased sensitivity to cofilin–mediated
387 filament severing (Bryan & Rubenstein, 2009). Interestingly, mutation p.P332A, close to the analyzed
388 mutation p.E334Q, enhances resistance towards cofilin–mediated severing (Bryan & Rubenstein,
389 2009). The perturbed cofilin interaction is the only overlap between the spectrum of molecular
390 phenotypes observed for syndromic deafness–associated mutations and mutation p.E334Q, which
391 results in a non–syndromic actinopathy. It has to be noted that all cited studies relied on the use of
392 actin purified from budding yeast for their biochemical studies, which shows 91% sequence identity to
393 human cytoskeletal γ–actin (Ng & Abelson, 1980).

394 Here, we describe mutation E334Q in cytoskeletal γ–actin that leads to a syndromic actinopathy with
395 hypotonia and is not associated with non–syndromic hearing loss. Our biochemical analysis shows that
396 the mutation does not affect the folding of the actin monomer or the stability of the monomer and the
397 resulting filaments, demonstrating that mutations in the hinge region do not necessarily affect protein
398 stability. The mutant protein displays a robust interaction with the VCA-activated Arp2/3 complex. Its
399 polymerization kinetics are equivalent to those of the WT protein, with which it effectively
400 copolymerizes *in vitro*. Based on these observations, we exclude functional haploinsufficiency as a
401 potential disease mechanism and favor a mechanism in which p.E334Q integrates into the cytoskeletal
402 actin networks of the cell but shows defects in the interaction with key binding partners. Consistent
403 with this hypothesis and based on several structural studies (Pospich *et al*, 2021; Behrmann *et al*, 2012;
404 Robert-Paganin *et al*, 2021; Risi *et al*, 2021; Fujii & Namba, 2017; Gyimesi *et al*, 2020; Gong *et al*, 2022;
405 Gurel *et al*, 2017; Von Der Ecken *et al*, 2016) as well as our initial modeling of complexes formed by
406 p.E334Q–filaments, we observed perturbed interactions with cofilin–1 and human cytoskeletal myosin
407 isoforms NM2A, NM2C and Myo5A (**Table 1**).

408 We interpret the observed changes in the interaction with NM2A, NM2C and Myo5A to primarily
409 reflect the weakening of complementary interactions between actin residue E334 and a core contact
410 triad in the myosin CM–loop, which in the case of NM2C consists of K429 and hydrophobic residues
411 I420 and V427 (**Figure 7**). Analogous changes in the interaction of mutant filaments with Myo1D,
412 Myo1G, NM2B, Myo5B, Myo5C and Myo19 are expected due to the presence of the core contact triad
413 residues in their CM–loops (**Figure 7B**). In contrast, the absence of a basic residue corresponding to
414 K429 in NM2C and additional changes affecting their CM loop structure make it difficult to predict the
415 consequences for the interaction of p.E334Q–filaments with the cytoskeletal myosin isoforms Myo1A,
416 Myo1C, Myo1E, Myo1F, Myo3A, Myo3B, Myo15, Myo18A, Myo18B and Myo19.

417 In addition to primary consequences, reflected in the observed changes in the binding interactions
418 with NM2A and cofilin–1, our results point to significant changes that result from allosteric
419 perturbations. The results from our transient–kinetic analysis of the complexes formed by p.E334Q
420 with NM2A–2R indicate that reduced allosteric coupling between the actin and nucleotide binding sites
421 within the myosin motor domain contributes to the observed decrease in motor activity. The coupling

422 efficiency is given by the ratio of the dissociation equilibrium constants for actin binding in the absence
423 (K_A) and presence of ADP (K_{DA}). The value for K_{DA}/K_D obtained for the interaction of NM2A–2R in the
424 presence of p.E334Q (20.9) is 3.5–fold lower than the value measured in the presence of WT actin
425 (Table 1). Allosteric perturbations are also major contributors mediating the impact of mutation E334Q
426 to the changes in elastic properties and the rate of actin filament disassembly in the presence of cofilin–
427 1. Our results are consistent with the E334Q mutation slowing the initial complex formation due to less
428 favorable charge interactions and allosteric perturbations having a major impact on subsequent steps.

429 Patients carrying mutations in *ACTB* or *ACTG1* predominately suffer from developmental disabilities,
430 which can be directly linked to cortical malformations of varying severity. Therefore, neuronal cells
431 and/or neuronal progenitor cells are assumed to be the most affected cell population in the patients
432 (Verloes *et al*, 2015; Di Donato *et al*, 2016; Rivière *et al*, 2012). The actin composition of the neuron is
433 thought to reach ratios between 1:1 and 1:2 for γ–actin to β–actin in the mature state after fluctuations
434 during neuronal development (Cheever & Ervasti, 2013). Studies of the spatial localization of the
435 cytoskeletal actin isoforms in the mature neuron are contradictory. A study showing that β– and
436 γ–actin strongly colocalize in hippocampal and cerebral neurons (Cheever *et al*, 2012) appears to
437 contradict previous studies, which reported spatial enrichment of β–actin in dynamic structures such
438 as the dendritic spine and exclusion from less dynamic structures such as the axon shaft, where γ–actin
439 was found to be enriched (Weinberger *et al*, 1996; Micheva *et al*, 1998; Bassell *et al*, 1998). Based on
440 our results, we conclude that p.E334Q actin is readily produced and integrated into the cytoskeletal
441 actin networks of neuronal cells, where it perturbs interactions with cytoskeletal myosin isoforms that
442 play essential roles in the function and maintenance of healthy neurons. The functions of myosin-5
443 isoforms in neuronal cells are all linked to their role as actin barbed-end directed processive cargo
444 transporters (Hammer & Wagner, 2013). Several of the myosin-5 driven transport-processes are
445 important contributors to synaptic plasticity, i.e. the ability of the neurons to change synaptic strength
446 based on previous activities (Hammer & Wagner, 2013).

447 The different NM2 isoforms are found in a wide range of cell types in the brain, but they show varying
448 spatial expressions (Murakami & Elzinga, 1992; Golomb *et al*, 2004; Rochlin *et al*, 1995; Kawamoto &
449 Adelstein, 1991). NM2A is predominately enriched in the vasculature of the brain, consistent with the
450 importance of NM2A for angiogenesis (Ma *et al*, 2020). NM2B and NM2C are mainly found in growth
451 cones and dendritic spines of neuronal cells (Murakami & Elzinga, 1992; Golomb *et al*, 2004; Rochlin *et*
452 *al*, 1995). NM2 isoforms are known to contribute to various neuronal processes, but unlike for Myo5A,
453 their exact role is less well understood. NM2B was shown to determine the maturation and
454 morphology of the dendritic spines in hippocampal neurons and was additionally linked to basal
455 synaptic function and plasticity (Hodges *et al*, 2011; Ma *et al*, 2004; Rex *et al*, 2010). NM2C and NM2B
456 contribute to the differentiation of oligodendrocytes (Domingues *et al*, 2020). The NM2 isoforms
457 compete with proteins of the ADF/cofilin family for binding to F–actin and this competition is essential
458 for stable actomyosin contractility and an intact cell cortex (Wiggan *et al*, 2012).

459 In line with this, ADF/cofilin family members are highly abundant in growth cones and dendritic spines
460 and essential for spine morphology and determination of spine length by modulating actin turnover
461 (Star *et al*, 2002; Hotulainen *et al*, 2009; Namme *et al*, 2021). Cofilin-mediated severing and nucleation
462 were previously proposed to synergistically contribute to global actin turnover in cells
463 (Andrianantoandro & Pollard, 2006; Du & Frieden, 1998). Our results show that the mutation affects
464 these different cofilin functions in actin dynamics in opposite ways. Cofilin-mediated filament
465 nucleation is more efficient for p.E334Q monomers, while cofilin-mediated severing of filaments

466 containing p.E334Q is significantly reduced. The interaction of both actin monomers and actin
467 filaments with ADF/cofilin proteins involves several distinct overlapping reactions. In the case of actin
468 filaments, cofilin binding is followed by structural modification of the filament, severing and
469 depolymerizing the filament (De La Cruz & Sept, 2010). Cofilin binding to monomeric actin is followed
470 by the closure of the nucleotide cleft and the formation of stabilized "long-pitch" actin dimers, which
471 stimulate nucleation (Andrianantoandro & Pollard, 2006).

472 While the number of disease–associated mutations reported for *ACTB* and *ACTG1* is steadily increasing,
473 the total number of patients affected remains low compared to patients with disease–associated
474 mutations in muscle actin isoforms (Parker *et al*, 2020). High sequence and structure conservation
475 across all actin isoforms enable us to extrapolate our findings obtained with cytoskeletal γ–actin to
476 diseases associated with mutations of E334 in other actin isoforms. Mutations of residue E334 in α–
477 skeletal actin (encoded by *ACTA1*) are reported to result in nemaline myopathy (E334K, (Laing *et al*,
478 2009)) or core myopathy (E334A, (Kaindl *et al*, 2004)) (reviewed in (Parker *et al*, 2020)). The mutations
479 either lead to the inversion of the charge at residue 334 (E334K) or the complete loss of charge (E334A).
480 Our study shows that loss of charge at actin residue 334 leads to the loss of a conserved core contact
481 between actin and the myosin motor domain of cytoskeletal class 2 myosin. Skeletal muscle myosin–2
482 is a central component of the sarcomere. The myosin forms the thick filaments that interact with the
483 thin filaments formed by actin and regulatory proteins, generating force that powers muscle
484 contraction (Sweeney & Hammers, 2018). Because the core contact triad that interacts with actin
485 residue E334 is present in all class 2 myosin isoforms, it is reasonable to assume that mutations of
486 residue E334 in α-skeletal actin affect the interaction with skeletal muscle myosin 2 to a similar extent,
487 resulting in less efficient force generation and thereby contributing to the development of myopathy
488 in patients.

489 Interestingly, a recent study analyzing the prevalence of cytoskeletal actin mutations in cancer using
490 the cBioPortal database found that mutations in *ACTB* and *ACTG1* are associated with lymphoid
491 cancers, specifically mutations in *ACTB* with diffuse large B–cell lymphoma and mutations in *ACTG1*
492 with multiple myeloma. When the authors extended the analysis to all cancer types, they found that
493 the observed mutations in the two genes were scattered across the entire actin sequence, with no
494 apparent preference for a particular region. Nevertheless, the group identified residue E334 in *ACTB*
495 as a potential hotspot, as the missense variants p.E334Q/p.E334K are more frequent in all analyzed
496 datasets (Witjes *et al*, 2020). In this paper, we investigated the impact of the E334Q exchange on the
497 function of cytoskeletal γ–actin in the context of developmental diseases. However, the high sequence
498 similarity between the cytoskeletal actin isoforms makes it highly likely that the E334Q mutation in
499 cytoskeletal β–actin results in similar molecular perturbations of actin dynamics but with potentially
500 different consequences for the organism due to varying enrichment of the two isoforms in functional
501 compartments of the actin cytoskeleton. Although future studies are needed to determine the role of
502 *ACTB* and *ACTG1* mutations as driver or passenger mutations in different cancers, our data show a
503 possible link between impaired cytoskeletal actomyosin dynamics, cofilin–mediated actin turnover and
504 cancer development.

505

506 # Material and Methods

507 ## Plasmids

508 The coding sequence of human cytoskeletal γ–actin (Uniprot-ID: P63261) was fused via a C–terminal
509 linker to a His_6–tagged thymosin β4 moiety (Uniprot-ID: P62328), as previously described for yeast
510 actin (Uniprot-ID: P60010) (Noguchi *et al*, 2007). The fusion protein was cloned into the multiple
511 cloning site of the pFastBac–Dual vector under the control of the polyhedrin promotor. The plasmid
512 encoding the mutant protein p.E334Q was generated by performing site-directed mutagenesis on the
513 WT plasmid. Motor domain carrying fragments of human NM2A, NM2C, and Myo5A were produced
514 using MYH9, MYH14, and MYO5A heavy chain sequences, respectively (Uniprot-IDs: P35579, Q7Z406,
515 Q9Y4I1). For the production of HMM-like constructs of human NM2A and human Myo5A, expression
516 vectors derived from pFastBac were used, as described previously (Hundt *et al*, 2016; Reindl *et al*,
517 2022). NM2A–HMM was co–produced with human light chains MYL6a (Uniprot-ID: P60660) and
518 MYL12b (Uniprot-ID: O14950). Myo5A HMM was co–produced with human calmodulin (Uniprot-ID:
519 P0DP23). NM2A–2R and NM2C–2R, single–headed, constitutively active motor domain constructs of
520 human NM2A and NM2C–2C0 with an artificial lever arm region, were produced using pFastBac–
521 derived expression vectors, as described previously (Heissler & Manstein, 2011; Müller *et al*, 2013).
522 Human cofilin–1 (Uniprot-ID: P23528) was cloned into the expression vector pGEX–6P–2 (Greve *et al*,
523 2022). The human Arp2/3 complex consisting of subunits Arp2 (Uniprot-ID: P61160), Arp3 (Uniprot-ID:
524 P61158), ArpC1B (Uniprot-ID: O15143, ArpC2 (Uniprot-ID: O15144), ArpC3A (Uniprot-ID: O15145),
525 ArpC4 (Uniprot-ID: P59998), ArpC5 (Uniprot-ID: O15511) and a C–terminal FLAG tag on ArpC3A was
526 produced using the expression vector pBIG2abc, provided by Roberto Dominguez (University of
527 Pennsylvania, Philadelphia, USA). The VCA domain of human N–WASP (Uniprot-ID: O00401) was
528 cloned into pGEX–6P–2. Human capping protein (subunits α1/β2, Uniprot-ID: P52907/P47756) in pET–
529 Duet–1 and eGFP–tagged human cofilin–1 (Uniprot-ID: P23528) in pGEX–6P–2 vector were provided
530 by Jan Faix (Medizinische Hochschule Hannover, Hannover, Germany). Recombinant bacmids and
531 viruses for the production of proteins in the Sf9 system were produced according to the *Bac–to–Bac*
532 baculovirus expression system protocol (Thermo Fisher Scientific, Waltham, MA, USA).

533

534 Protein production and purification

535 We produced recombinant human cytoskeletal γ–actin and p.E334Q mutant protein as actin–thymosin
536 β4–His_6 fusion protein using the baculovirus/*S. frugiperda* insect cell expression system. The C-terminal
537 native actin residue is a Phe, which provides a cleavage site for chymotrypsin to remove downstream
538 tag sequences completely. The tag sequence employed consists of a 14-amino acid linker
539 (ASSGGSGSGGSGGA), 43 thymosin-β4 residues, followed by 6 histidine residues. To produce WT and
540 mutant fusion proteins, 2×10^9 cells were harvested 72 hours after infection. Cells were pelleted,
541 washed with PBS, shock frozen in liquid nitrogen and stored at –80 °C. Cell pellets from two liters of
542 Sf–9 culture were thawed for a typical preparation. For lysis, cells were resuspended in lysis buffer–A
543 (10 mM Tris pH 7.8, 5 mM $CaCl_2$, 10 mM imidazole, 1.25% Triton X–100, 100 mM KCl, 7 mM β–
544 mercaptoethanol, 1 mM ATP, 1 mM PMSF, 100 µg/mL TAME, 80 µg/mL TPCK, 2 µg/mL pepstatin, 5
545 µg/mL leupeptin) and sonicated. The lysate was cleared by centrifugation at 30,000 × *g* (30 min, 4°C).
546 The cleared lysate was loaded onto 3 mL equilibrated PureCube 100 NiNTA agarose (Cube Biotech,
547 Manheim am Rhein, Germany) and incubated for two hours under constant rotation. Afterwards, the
548 material was washed extensively with 10 mM Tris pH 7.8, 0.2 mM $CaCl_2$, 10 mM imidazole, 50 mM KCl,
549 1 mM ATP and the actin–thymosin β4 fusion protein was eluted with 10 mM Tris pH 7.8, 250 mM
550 imidazole, 0.2 mM $CaCl_2$, 1 mM ATP. Peak fractions were pooled and dialyzed overnight against G–
551 buffer (10 mM Tris pH 7.8, 0.2 mM $CaCl_2$, 0.1 mM ATP, 0.5 mM DTT). The next day, protein aggregates

552 were removed by centrifugation at 15,000 × *g* (20 min, 4 °C). The supernatant was pooled and α–
553 chymotrypsin (Sigma-Aldrich, Schnelldorf, Germany) was added at a w/w ratio of 1:300
554 (chymotrypsin:actin) to remove the tag-sequences. The optimal digestion time varied from 45 to 80
555 min and needs to be determined for each batch of α–chymotrypsin. PMSF was added to a final
556 concentration of 0.2 mM to stop the digestion. Actin was separated from the thymosin-His tag using
557 polymerization-depolymerization steps. Unless otherwise stated, all protein purification steps were
558 carried out at 4°C. F-actin was stored on ice. G-actin was concentrated to approximately 150 µM, flash
559 frozen in liquid nitrogen and stored at –80°C in G–buffer. Clarified G-actin, free of aggregates and
560 oligomers, was always prepared fresh. G-actin stocks were thawed, diluted in G-buffer to the
561 appropriate concentration, and centrifuged at 136,000 × *g* (15 min, 4°C). The top 2/3 of the centrifuged
562 sample was carefully removed for use in further experiments. All myosin constructs were produced in
563 the baculovirus/*S. frugiperda* insect cell expression system and purified as previously described for
564 NM2A–HMM (Greve *et al*, 2022; Hundt *et al*, 2016; Pathan-Chhatbar *et al*, 2018), Myo5A–HMM (Reindl
565 *et al*, 2022), the single–headed, constitutively active constructs NM2A–2R (Heissler & Manstein, 2011;
566 Müller *et al*, 2013) and NM2C–2R (Heissler & Manstein, 2011; Müller *et al*, 2013). Production of the
567 human Arp2/3 complex in insect cells followed the procedure described in Zimmet *et al*. (Zimmet *et al*,
568 2020). Human cofilin–1 and human eGFP–cofilin–1 were produced as GST–fusion proteins in Rosetta2
569 (DE3) cells. Purification was carried out as previously described for human cofilin–1 (Greve *et al*, 2022).

570 Human GST–N–WASP–VCA was produced in ArcticExpress (DE3) cells. The cells were lysed by
571 treatment with lysozyme followed by sonification in lysis buffer–W (25 mM Tris pH 7.4, 50 mM NaCl,
572 1 mM EDTA, 1 mM DTT, 0.5% Triton X–100, 1 mM PMSF). The cleared cell lysate was loaded onto a
573 self–packed GSH–Sepharose column. The column was then washed with five column volumes of wash
574 buffer–W (25 mM TRIS pH 7.4, 50 mM NaCl, 1 mM EDTA, 1 mM DTT). GST–N–WASP–VCA was eluted
575 from the column by applying 10 mM glutathione in wash buffer–W. The eluted protein was
576 concentrated and loaded onto a S75 16/600 size exclusion chromatography column (GE Healthcare,
577 Chicago, USA). After chromatography, fractions containing pure protein were pooled, concentrated
578 and the concentration was determined via absorbance at 280 nm. The GST–N–WASP–VCA protein was
579 frozen in liquid nitrogen and stored at – 80°C.

580 Human capping protein (α1/β2) carrying a 6×His–tag was produced in Rosetta2 (DE3) cells. For
581 purification, cells were lysed by lysozyme followed by sonification in lysis buffer-CP (25 mM Tris pH 7.8,
582 250 mM NaCl, 1 mM EDTA, 1 mM PMSF, 1.5 % Triton X–100, 10 mM imidazole, 7 mM beta–
583 mercaptoethanol). The cleared lysate was loaded onto PureCube 100 NiNTA agarose (Cube Biotech,
584 Monheim am Rhein, Germany) in a gravity–flow column. The agarose was washed with wash buffer–
585 CP (25 mM Tris pH 7.8, 250 mM NaCl, 30 mM imidazole) and the protein was then eluted with elution
586 buffer–CP (25 mM Tris pH 7.8, 50 mM NaCl, 250 mM imidazole). Fractions with pure capping protein
587 were pooled, concentrated and loaded onto a S200 16/600 size exclusion chromatography column (GE
588 Healthcare, Chicago, USA). The purified protein was frozen in liquid nitrogen and stored at –80°C.

589 α–skeletal actin (Uniprot-ID: P68139) was prepared from chicken pectoralis major muscle, as
590 previously described for rabbit α–skeletal actin (Lehrer & Kerwar, 1972).

591 Unless otherwise stated, all purification steps were performed at 4°C.

592

593 DNase–I inhibition assay, DSF and nucleotide exchange assay

594 The DNase–I inhibition assay and DSF to study actin folding and thermal stability were performed as
595 previously described (Greve *et al*, 2022).

596 Nucleotide exchange experiments were performed with freshly clarified G–actin as follows. The G–
597 actin solution was passed through a Zeba™ spin desalting column (Thermo Fisher Scientific, Waltham,
598 MA, USA) equilibrated with G–buffer to remove excess nucleotide. The sample was then incubated
599 with a 2–fold excess of ε–ATP or ε–ADP (Jena Bioscience, Jena, Germany) for two hours on ice. After
600 incubation, excess nucleotide was removed by passing the sample through a Zeba™ spin desalting
601 column equilibrated with 10 mM TRIS pH 8.0 and 10 µM ε–ATP/ ε–ADP. The concentration of the Ca^{2+}–
602 ε–ATP/ε–ADP–G–actin solution was determined using the Coomassie protein assay (Thermo Fisher
603 Scientific, Waltham, MA, USA). Prior to the nucleotide exchange experiment the Ca^{2+}–ε–ATP/ε–ADP–
604 G–actin solution was supplemented with 10× Mg^{2+}-exchange buffer (1 mM $MgCl_2$, 10 mM EGTA) to a
605 final concentration of 0.1 mM $MgCl_2$ and 1 mM EGTA. The resulting solution was rapidly mixed 1:1 with
606 assay buffer–SF containing excess unlabeled ATP (10 mM TRIS pH 7.8, 0.2 mM $MgCl_2$, 0.2 mM ATP)
607 using a HiTech Scientific SF61 stopped–flow system (TgK Scientific Limited, Bradford on Avon, UK). The
608 ε–ATP/ε–ADP fluorescence was excited at 335 nm and monitored through a KV389 cut–off filter. The
609 displacement of the fluorescent nucleotide analogs by ATP results in a decrease in the fluorescence
610 amplitude, which is best described by a single exponential fit that yields the apparent rate of nucleotide
611 dissociation

612 CD spectroscopy

613 Directly prior to the measurement, the freshly clarified G-actin was diluted to 0.05 mg/mL in 10 mM
614 phosphate buffer pH 7.4. A buffer reference was prepared by mixing G buffer with 10 mM phosphate
615 buffer pH 7.4 in the same ratio. CD spectroscopy was performed with a PiStar 180 spectrometer
616 (Applied Photophysics, Leatherhead, UK). Measurements were performed at 25°C using quartz
617 cuvettes (0.3 cm path length) and nitrogen purging. CD spectra were recorded from 176 nm to 280 nm
618 in steps of 1 nm using a bandwidth of 4 nm. For every sample, three spectra were recorded and
619 subsequently averaged. The averaged buffer spectrum was subtracted, and the resulting protein
620 spectrum smoothed using a Savitsky–Golay filter (Savitzky & Golay, 1964) in two consecutive iterations.
621 The DichroWeb online platform was used to determine the secondary structure composition
622 (Whitmore & Wallace, 2004). Data were analyzed based on the mean residue ellipticity $[\theta]_{MRE}$ of the
623 sample using the CDSSTR algorithm and reference set 3 (optimized for 185 nm–240 nm).

624

625 Steady–state ATPase assay

626 The steady–state ATPase activity of F–actin was measured using a NADH–coupled enzymatic assay
627 (Furch *et al*, 1998). Experiments were performed with 10 µM F–actin at 37 °C in assay buffer–A (25 mM
628 HEPES pH 7.3, 5 mM $MgCl_2$, 50 mM KCl, 0.5 mM DTT) supplemented with the enzymatic system, which
629 generates the quantifiable readout (1 mM ATP, 0.5 mM NADH, 0.5 mM 2–phosphoenolpyruvate, 0.02
630 mg/mL lactate dehydrogenase from rabbit muscle (Sigma-Aldrich, Schnelldorf, Germany), 0.05 mg/mL
631 pyruvate kinase from rabbit muscle (Sigma-Aldrich, Schnelldorf, Germany), 0.5 mM NADH). For
632 measurements of the basal and actin–activated NM2A–HMM ATPase, 0.5 µM MLCK-treated HMM was
633 used. Phalloidin–stabilized WT or mutant F-actin was added over the range of 0–25 µM. The change in
634 absorbance at 340 nm due to oxidation of NADH was recorded in a Multiskan FC Microplate
635 Photometer (Thermo Fisher Scientific, Waltham, MA, USA). The data were fitted to the Michaelis-

636 Menten equation to obtain values for the actin concentration at half-maximal activation of ATP-
637 turnover (K_{app}) and for the maximum ATP-turnover at saturated actin concentration (k_{cat}).

638

639 TIRF microscopy–based assays

640 To distinguish between the impact of the mutation on filament nucleation and elongation, we
641 performed TIRF microscopy–based assays using freshly clarified protein. Unlabeled WT or mutant G–
642 actin was supplemented with 10% Atto–655 labeled WT or mutant G–actin for visualization of the
643 filament assembly process. Glass coverslips were cleaned, surfaces chemically treated and flow cells
644 assembled as described previously (Greve *et al*, 2022). To induce polymerization, the G–actin solutions
645 were diluted to a final concentration of 1 µM with 2× TIRF–buffer (20 mM imidazole, 50 mM KCl, 1 mM
646 $MgCl_2$, 1 mM EGTA, 0.2 mM ATP, 15 mM glucose, 20 mM β–ME, 0.25 % methylcellulose, 0.1 mg/mL
647 glucose oxidase and 0.02 mg/mL catalase. The solutions were mixed, immediately flushed into flow
648 cells and image acquisition was started.

649 To follow filament disassembly, two–color TIRF experiments with Atto–655 labeled actin and eGFP–
650 cofilin–1 were performed with preformed filaments that were "aged" and capped at their barbed end
651 by human capping protein. WT or mutant actin was polymerized for 3 hours at room temperature and
652 then moved to 4 °C overnight. "Aged" F–actin and human capping protein were diluted into TIRF–
653 buffer to generate capped actin filaments. eGFP–cofilin–1 was added to final concentrations of 300 nM
654 F–actin, 25 nM capping protein and 100 nM eGFP–cofilin–1. Immediately adding eGFP–cofilin–1, the
655 reaction mixture was flushed into the flow cell and image acquisition was started. Images were
656 captured using a Nikon Eclipse TI–E inverted microscope equipped with a 100×/1.49 NA Apo oil
657 immersion objective and Ixon3 897 EMCCD cameras (Andor, Belfast, UK) under control of the NIS
658 software (Nikon, Minato, Japan). Images were taken every 3 seconds with an exposure time of 60 ms.

659 To analyze actin polymerization in the presence of ABPs, the ABPs were first pre–diluted in KMEI buffer
660 and diluted to their final concentration in TIRF buffer just before adding actin. Image acquisition was
661 performed as described for experiments with actin only. Image analysis for all TIRF microscopy
662 experiments was performed using ImageJ (Rueden *et al*, 2017). The elongation rate of actin filaments
663 was determined by manually tracking individual filaments. Only filaments that could be tracked for at
664 least four consecutive minutes were used to determine the elongation rate. Using these criteria, 20 to
665 30 filaments were tracked in each individual experiment (in a microscopic field of view of 81.41 ×
666 81.41 µm). For quantification of two–color TIRFM–experiments, 52 × 52 µm ROIs from the entire
667 microscopic field of view were used. The number of filaments observed throughout an experiment was
668 determined using the *Analyze Particle* tool in ImageJ after background–subtraction (sliding paraboloid,
669 rolling ball radius: 25 pixels).

670

671 Unloaded *in vitro* motility assay

672 The unloaded *in vitro* motility assay to study the interaction between WT and mutant actin and NM2A–
673 HMM or Myo5A–HMM was essentially performed as previously described (Greve *et al*, 2022; Reindl *et*
674 *al*, 2022; Kron & Spudich, 1986). Flow cells used in the *in vitro* motility assay were constructed using
675 nitrocellulose–coated coverslips. NM2A–HMM requires phosphorylation of the associated regulatory
676 light chain for full enzymatic activity. Purified NM2A–HMM was incubated with the GST–tagged kinase
677 domain (residues 1425-1776) of human smooth muscle myosin light chain kinase (Uniprot-ID:

678 A0A8I5KU53) at a molar ratio of 10:1 in 25 mM MOPS, pH 7.3, 50 mM KCl, 5 mM $MgCl_2$, 1 mM $CaCl_2$,
679 0.2 µM calmodulin, 3 µM regulatory light chain (MLC12b), 3 µM essential light chain (MLC6a), 1 mM
680 DTT and 1 mM ATP for 30 minutes at 30 °C. In experiments with Myo5A–HMM, each buffer and actin
681 solution was supplemented with 2 µM calmodulin to prevent calmodulin dissociation from Myo5A–
682 HMM. Olympus IX70 or Olympus IX83 inverted fluorescence microscopes (Olympus, Hamburg,
683 Germany) equipped with a 60×/1.49 NA PlanApo oil immersion objective and an Orca Flash 4.0 CMOS
684 camera (Hamamatsu Photonics Deutschland GmbH, Herrsching, Germany) were used for image
685 acquisition. All *in vitro* motility experiments were performed at a 37°C. Analysis of the recorded image
686 series was performed in ImageJ (Rueden *et al*, 2017). The Plugin wrmTrck (Nussbaum-Krammer *et al*,
687 2015), developed by Jesper S. Pedersen, was used to determine the trajectories and corresponding
688 velocities of the individual actin filaments. Only filaments that showed movement for at least 30
689 consecutive seconds were tracked and used to determine the average sliding velocity.

690

691 Pyrene–actin based bulk–polymerization assays

692 The polymerization and depolymerization of pyrene–labeled recombinant WT or mutant actin (5%
693 pyrene-labeled WT or mutant actin) was monitored as a function of increasing or decreasing pyrene–
694 fluorescence using a Synergy 4™ microplate reader (BioTek Instruments, Winooski, VT, USA) and the
695 built–in filter set (Excitation: 340/30 nm, Emission: 400/30 nm) at 25 °C. For polymerization
696 experiments, 20 µL of a 10 µM solution of pyrene–labeled Mg^{2+}–ATP–G–actin (WT or mutant) was
697 placed in a black flat bottom 96–well plate (BrandTech Scientific, USA). 80 µL of 1.25 × polymerization
698 buffer (10 mM TRIS, pH 7.8, 100 mM KCl, 5 mM $MgCl_2$, 0.5 mM EGTA, 0.1 mM DTT and 0.1 mM ATP)
699 was added to the wells using the built–in pipetting function of the plate reader and the polymerization
700 of actin was followed as an increase in pyrene–fluorescence. For depolymerization experiments, 3 µL
701 of a 20 µM F–actin solution was placed in one well of the plate. The solution was rapidly diluted by the
702 addition of 297 µL G–buffer. The depolymerization of the filaments was monitored as a decrease in
703 pyrene–fluorescence.

704 The effects of Arp2/3 (+ GST–N–WASP–VCA) and cofilin–1 on filament assembly or disassembly were
705 analyzed by dispensing the actin solution and the ABP solution into the well by hand without mixing.
706 Polymerization buffer or G–buffer was added, the reaction components were thereby mixed and
707 recording of the ensuing changes in fluorescence intensity was started.

708 The bulk–polymerization rate was determined according to Doolittle *et al*. (Doolittle *et al*, 2013). A
709 linear regression was fitted to the linear region around the time–point of half–maximal fluorescence.
710 The depolymerization experiments were evaluated by fitting a single exponential function to the data,
711 including a linear component that accounts for bleaching.

712

713 Co–sedimentation experiments

714 Actin was polymerized at 20 µM for 3 hours at room temperature before being moved to 4 °C
715 overnight. For co–sedimentation experiments at pH 7.8, 5 µM of "aged" F–actin and varying
716 concentrations of human cofilin–1 were mixed in assay buffer–C (10 mM TRIS, pH 7.8, 100 mM KCl, 5
717 mM $MgCl_2$, 0.5 mM EGTA, 0.1 mM DTT and 0.1 mM ATP) to a final volume of 50 µL in 1.5 mL
718 polypropylene centrifuge tubes (Beckman Coulter, Brea, CA, USA) suited for high–speed centrifugation.
719 For experiments performed at pH 6.5, assay buffer–C was supplemented with piperazine–N,N'–bis(2–

720 ethanesulfonic acid) (PIPES, pH 6.5) to a final concentration of 100 mM to induce a pH shift from 7.8
721 to 6.5. Actin and cofilin–1 were added after the pH shift. Samples were incubated for 10 minutes at
722 23°C and then centrifuged at 136,000 × *g* (15 min, 4°C). The pellet and supernatant fractions were
723 subjected to SDS–PAGE and the gel was imaged at a ChemiDoc–MP–gel documentation system (Bio–
724 Rad Laboratories, Hercule, CA, USA). The amount of actin and cofilin–1 in the pellet and supernatant
725 was determined via densitometry using the Image Lab software (Bio–Rad Laboratories, Hercule, CA,
726 USA).

727

728 Transient kinetic analysis of the actomyosin complex

729 Myosin binding to pyrene–labeled actin leads to strong pyrene–fluorescence quenching. Mixing of the
730 rigor–pyrene–acto–NM2A–2R/NM2C–2R complex with an excess of unlabeled actin allows the
731 determination of k_{-A} (dissociation rate of myosin from F–actin in the absence of nucleotide). Prior to
732 the experiment, pyrene–labeled phalloidin–stabilized WT or mutant F–actin and the myosin solutions
733 were treated with apyrase (Merck KGaA, Darmstadt, Germany) to remove residual nucleotide. Pyrene–
734 labeled actin was mixed with a 1.5–fold excess of NM2A–2R/NM2C–2R in assay buffer–P (20 mM MOPS
735 pH 7.0, 100 mM KCl, 5 mM $MgCl_2$, 5 mM DTT) and incubated for 5 minutes on ice. The solution was
736 mixed with an excess of chicken α–skeletal actin in assay buffer–P to final concentrations of 0.5 µM
737 pyrene–labeled actin, 0.75 µM NM2A–2R and 5 µM α–skeletal actin. The solution was immediately
738 transferred into the well of a black 96–well microplate with a transparent bottom and a lid (Corning,
739 Corning, NY, USA). Fluorescence was excited at 365 nm and measured at 407 nm in a CLARIOstar Plus
740 microplate reader (BMG LABTECH, Offenburg, Germany) using bottom optics over 9 hours. The
741 dissociation rate (k_{-A}) of myosin from actin was determined by applying a single–exponential fit to the
742 data.

743 The apparent affinity of NM2A–2R to WT or mutant F–actin in the absence (K_A) or presence (K_{DA}) of
744 nucleotide was determined using the method developed by Kurzawa and Geeves (Kurzawa & Geeves,
745 1996). To determine K_A, all protein samples were treated with apyrase before the experiment. 100 nM
746 pyrene–labeled phalloidin–stabilized F–actin was incubated with increasing concentrations of NM2A–
747 2R (10–1,300 nM) for 5 minutes on ice in assay buffer–P without DTT. The solutions were shot against
748 20 µM ATP at a HiTech Scientific SF61 stopped–flow system (TgK Scientific Limited, Bradford on Avon,
749 UK) in a 1:1 ratio at 20 °C. Fluorescence was excited at 365 nm and recorded using a KV389 cut–off
750 filter. At least five transients were averaged for each concentration of NM2A–2R and fitted using a
751 single–exponential function. The relative fluorescence amplitudes were plotted against the pre–mix
752 myosin concentrations. The affinity was determined by applying a quadratic equation to the dataset,
753 where A is the amplitude, A_{max} the amplitude under saturation, [F–actin] the actin concentration prior
754 mix, [NM2A–2R] the variable NM2A–2R concentration and *K* the dissociation constant in the absence
755 or presence of nucleotide.

756 $$\mathrm{A} = \mathrm{A}_{\max} \times ([\mathrm{F-Actin}] + [\mathrm{NM2A-2R}] + K) - \sqrt{\frac{([\mathrm{F-Actin}] + [\mathrm{NM2A-2R}] + K)^2 - 4 \times [\mathrm{F-Actin}] \times [\mathrm{NM2A-2R}]}{2 \times [\mathrm{F-Actin}]}}$$

757

758 Slight modifications of the experimental protocol were necessary to determine K_{DA}. Incubation with
759 apyrase was omitted, instead the pyrene–actomyosin complex was incubated with 30 µM ADP (Merck
760 KGaA, Darmstadt, Germany) for 20 minutes on ice prior to measurement. To account for the lower
761 affinity in the presence of ADP, the range of used myosin concentrations was extended up to 3,000

762 nM. Additionally, the concentration of ATP in the mixing experiment was increased to 300 µM pre–
763 mix. Data was recorded and evaluated as done for experiments without nucleotide.

764 The apparent ATP–affinity of the actomyosin complex was determined by mixing the apyrase–treated,
765 pyrene–labeled, phalloidin–stabilized actomyosin complex with increasing concentrations of ATP at
766 the stopped–flow system. Fitting an exponential function to the individual transients yields the ATP–
767 dependent dissociation rate of NM2A–2R from F–actin (k_{obs}). The k_{obs}–values were plotted against the
768 corresponding ATP concentrations and a hyperbola was fitted to the data. The fit yields the apparent
769 ATP–affinity ($1/K_1$) of the actomyosin complex and the maximal dissociation rate k_{+2}. The apparent
770 second–order rate constant for ATP binding (K_1k_{+2}) was determined by applying a linear fit to the data
771 obtained at low ATP concentrations (0 – 25 µM).

772

773 Molecular modelling

774 Homology models of human cytoskeletal γ–actin, human cofilin–1 and the human NM2A motor
775 domain were generated with MODELLER (Sali & Blundell, 1993). Models of filamentous human
776 cytoskeletal γ–actin with bound cofilin–1 or NM2A motor domain were generated based on cryo–EM
777 structures obtained from the Protein Data Bank of the barbed end side of a cofilactin cluster (pdb:
778 6UC4, 6UBY, 6VAO) (Huehn *et al*, 2020) and a human cytoplasmic actomyosin complex (pdb: 5JLH)
779 (Von Der Ecken *et al*, 2016). The structures were accessed on May 25, 2023. Mutation E334Q was
780 introduced using the mutagenesis tool in PyMOL (Schrödinger, LLC, 2015). PyMOL and ChimeraX
781 (Goddard *et al*, 2018; Pettersen *et al*, 2021) were used for distance measurements and visualization of
782 Coulomb surfaces.
783 Identification and alignment of the CM–loop region of cytoskeletal myosin isoforms were performed
784 using the match function of ChimeraX, by superimposing and aligning cytoskeletal myosin isoform
785 structures on NM2C (pdb-NM2C: 5JLH, pdb-Myo5A: 7PM5, pdb-Myo5C: 5HMP, pdb-Myo1D: AF-
786 O94832-F1, pdb-Myo15: 7UDT, pdb-Myo19: AF-Q96H55-F1). Where appropriate, the corresponding
787 human sequences were retrieved from UniProt and structurally aligned.
788 Normal mode analyses (NMA) were performed using the Elastic Network Model (ENM) elNémo (Suhre
789 & Sanejouand, 2004) and an nrbl value of 5.
790

791 Data Analysis

792 Data analysis and graph plotting were performed with Origin 2023 (OriginLab Corporation.
793 Massachusetts, USA). Errors are given as standard deviation (SD) based on three independent
794 experiments if not otherwise specified. The significance of the data was evaluated in Origin 2023 using
795 a two–sample t–test ($p > 0.05$ ≙ ns, $p \leq 0.05$ ≙ *, $p \leq 0.01$ ≙ **, $p \leq 0.001$ ≙ ***, $p \leq 0.0001$ ≙ ****).

796

797 Author Contributions

798 All authors discussed the results and contributed to the final manuscript; J.N.G., T.R., C.T. purified
799 proteins; J.N.G. performed experiments; A.M. and R.H. performed *in silico* studies; J.N.G. and D.J.M.
800 analyzed the data; J.N.G., M.H.T., N.D.D. and D.J.M. contributed to the experimental design; J.N.G.,
801 A.M., R.H. and D.J.M. designed figures; J.N.G. and D.J.M. conceived and coordinated the study, and

802 wrote the manuscript; D.J.M. was responsible for funding acquisition, supervision and project
803 administration.

804

805 Acknowledgments

806 The authors thank Roberto Dominguez (University of Pennsylvania, Philadelphia, USA) for providing
807 vector pBIGBac–Arp2/3 and Jan Faix (Medizinische Hochschule Hannover, Hannover, Germany) for
808 providing vectors pGEX–eGFP–cofilin–1 and pETDuet–CP.

809 D.J.M was supported by grants from Deutsche Forschungsgemeischaft (DFG) (MA1081/23-1,
810 MA1081/28-1), J.N.G., A.M., N.DD and D.J.M. are members of the European Union's Horizon 2020
811 research and innovation program under the EJP RD COFUND–EJP N° 825575 with support from the
812 German Federal Ministry of Education and Research under Grant Agreement 01GM1922B. D.J.M. is a
813 member of the Cluster of Excellence RESIST (EXC 2155; DFG–Project ID: 39087428–B11). J.N.G. is
814 supported by the HiLF I grant for early career researcher from Medizinische Hochschule Hannover. We
815 gratefully acknowledge support provided by the Core Unit for Structural Biochemistry, the Core Unit
816 for Laser Microscopy at MHH. Computing time was provided on supercomputers Lise and Emmy at
817 NHR@ZIB and NHR@Göttingen, as part of the Alliance for National High Performance Computing
818 (NHR) infrastructure. The calculations for this research were conducted with computing resources
819 under the project ID nib00018. T.R. was enrolled in the PhD program Molecular Medicine of Hannover
820 Biomedical Research School (HBRS).

821

Literature

Abercrombie M, Heaysman JEM & Pegrum SM (1971) The locomotion of fibroblasts in culture: IV. Electron microscopy of the leading lamella. *Exp Cell Res* 67: 359–367

Abercrombie M, Joan E, Heaysman M & Pegrum SM (1970) The locomotion of fibroblasts in culture: II. “Ruffling”. *Exp Cell Res* 60: 437–444

Andrianantoandro E & Pollard TD (2006) Mechanism of Actin Filament Turnover by Severing and Nucleation at Different Concentrations of ADF/Cofilin. *Mol Cell* 24

Anson M, Geeves MA, Kurzawa SE & Manstein DJ (1996) Myosin motors with artificial lever arms. *EMBO J* 15: 6069–6074

Baraitser M & Winter RM (1988) Iris coloboma, ptosis, hypertelorism, and mental retardation: a new syndrome. *J Med Genet* 25: 41–43

Bassell GJ, Zhang H, Byrd AL, Femino AM, Singer RH, Taneja KL, Lifshitz LM, Herman IM & Kosik KS (1998) Sorting of beta-actin mRNA and protein to neurites and growth cones in culture. *J Neurosci Off J Soc Neurosci* 18: 251–265

Behrmann E, Müller M, Penczek PA, Mannherz HG, Manstein DJ & Raunser S (2012) Structure of the rigor actin-tropomyosin-myosin complex. *Cell* 150: 327–338

Blanchoin L, Amann KJ, Higgs HN, Marchand J-B, Kaiser DA & Pollard TD (2000) Direct observation of dendritic actin filament networks nucleated by Arp2/3 complex and WASP/Scar proteins. *Nature* 404: 1007–1011

Blanchoin L & Pollard TD (1999) Mechanism of interaction of Acanthamoeba actophorin (ADF/Cofilin) with actin filaments. *J Biol Chem* 274: 15538–15546

Breitsprecher D, Koestler SA, Chizhov I, Nemethova M, Mueller J, Goode BL, Small JV, Rottner K & Faix J (2011) Cofilin cooperates with fascin to disassemble filopodial actin filaments. *J Cell Sci* 124: 3305–3318

Bryan KE & Rubenstein PA (2009) Allele-specific effects of human deafness γ-actin mutations (DFNA20/26) on the actin/cofilin interaction. *J Biol Chem* 284

Bryan KE, Wen KK, Zhu M, Rendtorff ND, Feldkamp M, Tranebjaerg L, Friderici KH & Rubenstein PA (2006) Effects of human deafness γ-actin mutations (DFNA20/26) on actin function. *J Biol Chem* 281

Cheever TR & Ervasti JM (2013) Actin isoforms in neuronal development and function. *Int Rev Cell Mol Biol* 301: 157–213

Cheever TR, Li B & Ervasti JM (2012) Restricted Morphological and Behavioral Abnormalities following Ablation of β-Actin in the Brain. *PLoS ONE* 7: e32970

Cope MJT, Whisstock J, Rayment I & Kendrick-Jones J (1996) Conservation within the myosin motor domain: implications for structure and function. *Structure* 4: 969–987

Costa CF, Rommelaere H, Waterschoot D, Sethi KK, Nowak KJ, Laing NG, Ampe C & Machesky LM (2004) Myopathy mutations in alpha-skeletal-muscle actin cause a range of molecular defects. *J Cell Sci* 117: 3367–3377

Cuvertino S, Stuart HM, Chandler KE, Roberts NA, Armstrong R, Bernardini L, Bhaskar S, Callewaert B, Clayton-Smith J, Davalillo CH, *et al* (2017) ACTB Loss-of-Function Mutations Result in a Pleiotropic Developmental Disorder. *Am J Hum Genet*

De La Cruz EM (2005) Cofilin Binding to Muscle and Non-muscle Actin Filaments: Isoform-dependent Cooperative Interactions. *J Mol Biol* 346: 557–564

De La Cruz EM & Sept D (2010) The Kinetics of Cooperative Cofilin Binding Reveals Two States of the Cofilin-Actin Filament. *Biophys J* 98: 1893–1901

De La Cruz EM, Wells AL, Rosenfeld SS, Ostap EM & Sweeney HL (1999) The kinetic mechanism of myosin V. *Proc Natl Acad Sci* 96: 13726–13731

Di Donato N, Kuechler A, Vergano S, Heinritz W, Bodurtha J, Merchant SR, Breningstall G, Ladda R, Sell S, Altmüller J, *et al* (2016) Update on the ACTG1-associated Baraitser–Winter cerebrofrontofacial syndrome. *Am J Med Genet A* 170

Di Donato N, Rump A, Koenig R, Der Kaloustian VM, Halal F, Sonntag K, Krause C, Hackmann K, Hahn G, Schrock E, *et al* (2014) Severe forms of Baraitser-Winter syndrome are caused by ACTB mutations rather than ACTG1 mutations. *Eur J Hum Genet* 22: 179–183

Domingues HS, Urbanski MM, Macedo-Ribeiro S, Almaktari A, Irfan A, Hernandez Y, Wang H, Relvas JB, Rubinstein B, Melendez-Vasquez CV, *et al* (2020) Pushing myelination – developmental regulation of myosin expression drives oligodendrocyte morphological differentiation. *J Cell Sci* 133: jcs232264

Dominguez R & Holmes KC (2011) Actin Structure and Function. *Annu Rev Biophys* 40: 169–186

Doolittle LK, Rosen MK & Padrick SB (2013) Measurement and analysis of in vitro actin polymerization. *Methods Mol Biol* 1046

Du J & Frieden C (1998) Kinetic Studies on the Effect of Yeast Cofilin on Yeast Actin Polymerization. *Biochemistry* 37: 13276–13284

Dugina V, Khromova N, Rybko V, Blizniukov O, Shagieva G, Chaponnier C, Kopnin B & Kopnin P (2015) Tumor promotion by γ and suppression by β non-muscle actin isoforms. *Oncotarget* 6: 14556–14571

Dugina V, Zwaenepoel I, Gabbiani G, Clément S & Chaponnier C (2009) Beta and gamma-cytoplasmic actins display distinct distribution and functional diversity. *J Cell Sci* 122: 2980–8

Fujii T & Namba K (2017) Structure of actomyosin rigour complex at 5.2 Å resolution and insights into the ATPase cycle mechanism. *Nat Commun* 8: 13969

Furch M, Geeves MA & Manstein DJ (1998) Modulation of Actin Affinity and Actomyosin Adenosine Triphosphatase by Charge Changes in the Myosin Motor Domain. *Biochemistry* 37: 6317–6326

Goddard TD, Huang CC, Meng EC, Pettersen EF, Couch GS, Morris JH & Ferrin TE (2018) UCSF ChimeraX: Meeting modern challenges in visualization and analysis. *Protein Sci Publ Protein Soc* 27: 14–25

Goley ED & Welch MD (2006) The ARP2/3 complex: an actin nucleator comes of age. *Nat Rev Mol Cell Biol* 7: 713–726

Golomb E, Ma X, Jana SS, Preston YA, Kawamoto S, Shoham NG, Goldin E, Conti MA, Sellers JR & Adelstein RS (2004) Identification and characterization of nonmuscle myosin II-C, a new member of the myosin II family. *J Biol Chem* 279: 2800–2808

Gong R, Jiang F, Moreland ZG, Reynolds MJ, de los Reyes SE, Gurel P, Shams A, Heidings JB, Bowl MR, Bird JE, *et al* (2022) Structural basis for tunable control of actin dynamics by myosin-15 in mechanosensory stereocilia. *Sci Adv* 8: eabl4733

Greve JN, Schwäbe FV, Pokrant T, Faix J, Di Donato N, Taft MH & Manstein DJ (2022) Frameshift mutation S368fs in the gene encoding cytoskeletal β-actin leads to ACTB-associated syndromic thrombocytopenia by impairing actin dynamics. *Eur J Cell Biol* 101: 151216

Gurel PS, Kim LY, Ruijgrok PV, Omabegho T, Bryant Z & Alushin GM (2017) Cryo-EM structures reveal specialization at the myosin VI-actin interface and a mechanism of force sensitivity. *eLife* 6: e31125

Gyimesi M, Horváth ÁI, Túrós D, Suthar SK, Pénzes M, Kurdi C, Canon L, Kikuti C, Ruppel KM, Trivedi DV, *et al* (2020) Single Residue Variation in Skeletal Muscle Myosin Enables Direct and Selective Drug Targeting for Spasticity and Muscle Stiffness. *Cell* 183: 335-346.e13

Hammer JA & Wagner W (2013) Functions of Class V Myosins in Neurons. *J Biol Chem* 288: 28428–28434

Heissler SM & Manstein DJ (2011) Comparative kinetic and functional characterization of the motor domains of human nonmuscle myosin-2C isoforms. *J Biol Chem* 286: 21191–21202

Hodges JL, Newell-Litwa K, Asmussen H, Vicente-Manzanares M & Horwitz AR (2011) Myosin IIB Activity and Phosphorylation Status Determines Dendritic Spine and Post-Synaptic Density Morphology. *PLOS ONE* 6: e24149

Hotulainen P, Llano O, Smirnov S, Tanhuanpää K, Faix J, Rivera C & Lappalainen P (2009) Defining mechanisms of actin polymerization and depolymerization during dendritic spine morphogenesis. *J Cell Biol* 185: 323–339

Huehn AR, Bibeau JP, Schramm AC, Cao W, De La Cruz EM & Sindelar CV (2020) Structures of cofilin-induced structural changes reveal local and asymmetric perturbations of actin filaments. *Proc Natl Acad Sci U S A* 117

Hundt N, Preller M, Swolski O, Ang AM, Mannherz HG, Manstein DJ & Müller M (2014) Molecular mechanisms of disease-related human β-actin mutations p.R183W and p.E364K. *FEBS J* 281: 5279–5291

Hundt N, Steffen W, Pathan-Chhatbar S, Taft MH & Manstein DJ (2016) Load-dependent modulation of non-muscle myosin-2A function by tropomyosin 4.2. *Sci Rep* 6: 20554

Ilkovski B, Nowak KJ, Domazetovska A, Maxwell AL, Clement S, Davies KE, Laing NG, North KN & Cooper ST (2004) Evidence for a dominant-negative effect in ACTA1 nemaline myopathy caused by abnormal folding, aggregation and altered polymerization of mutant actin isoforms. *Hum Mol Genet* 13: 1727–1743

Jepsen L, Kruth KA, Rubenstein PA & Sept D (2016) Two Deafness-Causing Actin Mutations (DFNA20/26) Have Allosteric Effects on the Actin Structure. *Biophys J* 111

Kaindl AM, Rüschendorf F, Krause S, Goebel H-H, Koehler K, Becker C, Pongratz D, Müller-Höcker J, Nürnberg P, Stoltenburg-Didinger G, *et al* (2004) Missense mutations of ACTA1 cause dominant congenital myopathy with cores. *J Med Genet* 41: 842–848

Kawamoto S & Adelstein RS (1991) Chicken nonmuscle myosin heavy chains: differential expression of two mRNAs and evidence for two different polypeptides. *J Cell Biol* 112: 915–924

Kron SJ & Spudich JA (1986) Fluorescent actin filaments move on myosin fixed to a glass surface. *Proc Natl Acad Sci* 83: 6272–6276

Kruth KA & Rubenstein PA (2012) Two deafness-causing (DFNA20/26) actin mutations affect Arp2/3-dependent actin regulation. *J Biol Chem* 287: 27217–27226

Kurzawa SE & Geeves MA (1996) A novel stopped-flow method for measuring the affinity of actin for myosin head fragments using μg quantities of protein. *J Muscle Res Cell Motil* 17: 669–676

Laing NG, Dye DE, Wallgren-Pettersson C, Richard G, Monnier N, Lillis S, Winder TL, Lochmüller H, Graziano C, Mitrani-Rosenbaum S, *et al* (2009) Mutations and polymorphisms of the skeletal muscle α-actin gene (ACTA1). *Hum Mutat* 30: 1267–1277

Latham SL, Chaponnier C, Dugina V, Couraud P-O, Grau GER & Combes V (2013) Cooperation between β- and γ-cytoplasmic actins in the mechanical regulation of endothelial microparticle formation. *FASEB J* 27: 672–683

Latham SL, Ehmke N, Reinke PYA, Taft MH, Eicke D, Reindl T, Stenzel W, Lyons MJ, Friez MJ, Lee JA, *et al* (2018) Variants in exons 5 and 6 of ACTB cause syndromic thrombocytopenia. *Nat Commun* 9

Lauffenburger DA & Horwitz AF (1996) Cell Migration: A Physically Integrated Molecular Process. *Cell* 84: 359–369

Lehrer SS & Kerwar G (1972) Intrinsic fluorescence of actin. *Biochemistry* 11: 1211–1217

Loisel TP, Boujemaa R, Pantaloni D & Carlier MF (1999) Reconstitution of actin-based motility of Listeria and Shigella using pure proteins. *Nature* 401: 613–616

Lu H, Fagnant PM, Bookwalter CS, Joel P & Trybus KM (2015) Vascular disease-causing mutation R258C in ACTA2 disrupts actin dynamics and interaction with myosin. *Proc Natl Acad Sci U S A* 112: E4168-4177

Ma X, Kawamoto S, Hara Y & Adelstein RS (2004) A point mutation in the motor domain of nonmuscle myosin II-B impairs migration of distinct groups of neurons. *Mol Biol Cell* 15: 2568–2579

Ma X, Uchida Y, Wei T, Liu C, Adams RH, Kubota Y, Gutkind JS, Mukouyama Y & Adelstein RS (2020) Nonmuscle myosin 2 regulates cortical stability during sprouting angiogenesis. *Mol Biol Cell* 31: 1974–1987

McCormack EA, Llorca O, Carrascosa JL, Valpuesta JM & Willison KR (2001a) Point mutations in a hinge linking the small and large domains of beta-actin result in trapped folding intermediates bound to cytosolic chaperonin CCT. *J Struct Biol* 135: 198–204

McCormack EA, Rohman MJ & Willison KR (2001b) Mutational screen identifies critical amino acid residues of β-actin mediating interaction between its folding intermediates and eukaryotic cytosolic chaperonin CCT. *J Struct Biol* 135

Micheva KD, Vallée A, Beaulieu C, Herman IM & Leclerc N (1998) beta-Actin is confined to structures having high capacity of remodelling in developing and adult rat cerebellum. *Eur J Neurosci* 10: 3785–3798

Morín M, Bryan KE, Mayo-Merino F, Goodyear R, Mencía Á, Modamio-Høybjør S, Del Castillo I, Cabalka JM, Richardson G, Moreno F, *et al* (2009) In vivo and in vitro effects of two novel gamma-actin (ACTG1) mutations that cause DFNA20/26 hearing impairment. *Hum Mol Genet* 18

Müller M, Diensthuber RP, Chizhov I, Claus P, Heissler SM, Preller M, Taft MH & Manstein DJ (2013) Distinct Functional Interactions between Actin Isoforms and Nonsarcomeric Myosins. *PLoS ONE* 8

Müller M, Mazur AJ, Behrmann E, Diensthuber RP, Radke MB, Qu Z, Littwitz C, Raunser S, Schoenenberger C-A, Manstein DJ, *et al* (2012) Functional characterization of the human α-cardiac actin mutations Y166C and M305L involved in hypertrophic cardiomyopathy. *Cell Mol Life Sci CMLS* 69: 3457–3479

Mullins RD, Heuser JA & Pollard TD (1998) The interaction of Arp2/3 complex with actin: Nucleation, high affinity pointed end capping, and formation of branching networks of filaments. *Proc Natl Acad Sci*

Murakami N & Elzinga M (1992) Immunohistochemical studies on the distribution of cellular myosin II isoforms in brain and aorta. *Cell Motil* 22: 281–295

Namme JN, Bepari AK & Takebayashi H (2021) Cofilin Signaling in the CNS Physiology and Neurodegeneration. *Int J Mol Sci* 22: 10727

Ng R & Abelson J (1980) Isolation and sequence of the gene for actin in Saccharomyces cerevisiae. *Proc Natl Acad Sci U S A* 77: 3912–3916

Nicholson-Dykstra S, Higgs HN & Harris ES (2005) Actin Dynamics: Growth from Dendritic Branches. *Curr Biol* 15: R346–R357

Noguchi TQP, Kanzaki N, Ueno H, Hirose K & Uyeda TQP (2007) A novel system for expressing toxic actin mutants in Dictyostelium and purification and characterization of a dominant lethal yeast actin mutant. *J Biol Chem*

Noguchi TQP, Komori T, Umeki N, Demizu N, Ito K, Iwane AH, Tokuraku K, Yanagida T & Uyeda TQP (2012) G146V Mutation at the Hinge Region of Actin Reveals a Myosin Class-specific Requirement of Actin Conformations for Motility*. *J Biol Chem* 287: 24339–24345

Nussbaum-Krammer CI, Neto MF, Brielmann RM, Pedersen JS & Morimoto RI (2015) Investigating the spreading and toxicity of prion-like proteins using the metazoan model organism C. elegans. *J Vis Exp JoVE*: 52321

Oda T, Iwasa M, Aihara T, Maéda Y & Narita A (2009) The nature of the globular- to fibrous-actin transition. *Nature* 457

Parker F, Baboolal TG & Peckham M (2020) Actin mutations and their role in disease. *Int J Mol Sci* 21

Pathan-Chhatbar S, Taft MH, Reindl T, Hundt N, Latham SL & Manstein DJ (2018) Three mammalian tropomyosin isoforms have different regulatory effects on nonmuscle myosin-2B and filamentous β-actin in vitro. *J Biol Chem* 293: 863–875

Pavlyk I, Leu NA, Vedula P, Kurosaka S & Kashina A (2018) Rapid and dynamic arginylation of the leading edge β-actin is required for cell migration. *Traffic* 19

Pettersen EF, Goddard TD, Huang CC, Meng EC, Couch GS, Croll TI, Morris JH & Ferrin TE (2021) UCSF ChimeraX: Structure visualization for researchers, educators, and developers. *Protein Sci Publ Protein Soc* 30: 70–82

Plastino J & Blanchoin L (2019) Dynamic stability of the actin ecosystem. *J Cell Sci* 132

Pollard TD (2016) Actin and actin-binding proteins. *Cold Spring Harb Perspect Biol* 8

Pollard TD, Blanchoin L & Mullins RD (2002) Molecular Mechanisms Controlling Actin Filament Dynamics in Nonmuscle Cells. *Annu Rev Biophys Biomol Struct*

Ponti A, Machacek M, Gupton SL, Waterman-Storer CM & Danuser G (2004) Two Distinct Actin Networks Drive the Protrusion of Migrating Cells. *Science* 305: 1782–1786

Pope BJ, Gonsior SM, Yeoh S, McGough A & Weeds AG (2000) Uncoupling actin filament fragmentation by cofilin from increased subunit turnover. *J Mol Biol* 298: 649–661

Pospich S, Sweeney HL, Houdusse A & Raunser S (2021) High-resolution structures of the actomyosin-V complex in three nucleotide states provide insights into the force generation mechanism. *eLife* 10: e73724

Reindl T, Giese S, Greve JN, Reinke PY, Chizhov I, Latham SL, Mulvihill DP, Taft MH & Manstein DJ (2022) Distinct actin–tropomyosin cofilament populations drive the functional diversification of cytoskeletal myosin motor complexes. *iScience* 25: 104484

Rendtorff NDND, Zhu M, Fagerheim T, Antal TL, Jones MP, Teslovich TM, Gillanders EM, Barmada M, Teig E, Trent JM, *et al* (2006) A novel missense mutation in ACTG1 causes dominant deafness in a Norwegian DFNA20/26 family, but ACTG1 mutations are not frequent among families with hereditary hearing impairment. *Eur J Hum Genet*

Rex CS, Gavin CF, Rubio MD, Kramar EA, Chen LY, Jia Y, Huganir RL, Muzyczka N, Gall CM, Miller CA, *et al* (2010) Myosin IIb regulates actin dynamics during synaptic plasticity and memory formation. *Neuron* 67: 603–617

Ridley AJ, Schwartz MA, Burridge K, Firtel RA, Ginsberg MH, Borisy G, Parsons JT & Horwitz AR (2003) Cell Migration: Integrating Signals from Front to Back. *Science* 302: 1704–1709

Risi C, Schäfer LU, Belknap B, Pepper I, White HD, Schröder GF & Galkin VE (2021) High-Resolution Cryo-EM Structure of the Cardiac Actomyosin Complex. *Structure* 29: 50-60.e4

Rivière JB, Van Bon BWM, Hoischen A, Kholmanskikh SS, O'Roak BJ, Gilissen C, Gijsen S, Sullivan CT, Christian SL, Abdul-Rahman OA, *et al* (2012) De novo mutations in the actin genes ACTB and ACTG1 cause Baraitser-Winter syndrome. *Nat Genet* 44: 440–444

Robert-Paganin J, Xu X-P, Swift MF, Auguin D, Robblee JP, Lu H, Fagnant PM, Krementsova EB, Trybus KM, Houdusse A, *et al* (2021) The actomyosin interface contains an evolutionary conserved core and an ancillary interface involved in specificity. *Nat Commun* 12: 1892

Rochlin MW, Itoh K, Adelstein RS & Bridgman PC (1995) Localization of myosin II A and B isoforms in cultured neurons. *J Cell Sci* 108 (Pt 12): 3661–3670

Rueden CT, Schindelin J, Hiner MC, DeZonia BE, Walter AE, Arena ET & Eliceiri KW (2017) ImageJ2: ImageJ for the next generation of scientific image data. *BMC Bioinformatics* 18: 529

Sali A & Blundell TL (1993) Comparative protein modelling by satisfaction of spatial restraints. *J Mol Biol* 234: 779–815

Savitzky Abraham & Golay MJE (1964) Smoothing and Differentiation of Data by Simplified Least Squares Procedures. *Anal Chem* 36: 1627–1639

Schröder JM, Durling H & Laing N (2004) Actin myopathy with nemaline bodies, intranuclear rods, and a heterozygous mutation in ACTA1 (Asp154Asn). *Acta Neuropathol (Berl)* 108: 250–256

Schrödinger, LLC (2015) The PyMOL Molecular Graphics System, Version 1.8.

Schüler H, Lindberg U, Schutt CE & Karlsson R (2000) Thermal unfolding of G-actin monitored with the DNase I-inhibition assay. *Eur J Biochem*

Sellers JR (2000) Myosins: a diverse superfamily. *Biochim Biophys Acta BBA - Mol Cell Res* 1496: 3–22

Star EN, Kwiatkowski DJ & Murthy VN (2002) Rapid turnover of actin in dendritic spines and its regulation by activity. *Nat Neurosci* 5: 239–246

Suhre K & Sanejouand Y-H (2004) ElNemo: a normal mode web server for protein movement analysis and the generation of templates for molecular replacement. *Nucleic Acids Res* 32: W610-614

Sweeney HL & Hammers DW (2018) Muscle Contraction. *Cold Spring Harb Perspect Biol* 10: a023200

Vang S, Corydon TJ, Børglum AD, Scott MD, Frydman J, Mogensen J, Gregersen N & Bross P (2005) Actin mutations in hypertrophic and dilated cardiomyopathy cause inefficient protein folding and perturbed filament formation. *FEBS J* 272

Vedula P, Kurosaka S, Leu NA, Wolf YI, Shabalina SA, Wang J, Sterling S, Dong DW & Kashina A (2017) Diverse functions of homologous actin isoforms are defined by their nucleotide, rather than their amino acid sequence. *eLife* 6

Verloes A, Di Donato N, Masliah-Planchon J, Jongmans M, Abdul-Raman OA, Albrecht B, Allanson J, Brunner H, Bertola D, Chassaing N, *et al* (2015) Baraitser-Winter cerebrofrontofacial syndrome: Delineation of the spectrum in 42 cases. *Eur J Hum Genet* 23: 292–301

Von Der Ecken J, Heissler SM, Pathan-Chhatbar S, Manstein DJ & Raunser S (2016) Cryo-EM structure of a human cytoplasmic actomyosin complex at near-atomic resolution. *Nature* 534: 724–728

Weinberger R, Schevzov G, Jeffrey P, Gordon K, Hill M & Gunning P (1996) The molecular composition of neuronal microfilaments is spatially and temporally regulated. *J Neurosci Off J Soc Neurosci* 16: 238–252

Whitmore L & Wallace BA (2004) DICHROWEB, an online server for protein secondary structure analyses from circular dichroism spectroscopic data. *Nucleic Acids Res* 32: W668–W673

Wiggan O, Shaw AE, DeLuca JG & Bamburg JR (2012) ADF/Cofilin Regulates Actomyosin Assembly through Competitive Inhibition of Myosin II Binding to F-Actin. *Dev Cell* 22: 530–543

van Wijk E, Krieger E, Kemperman MH, De Leenheer EMR, Huygen PLM, Cremers CWRJ, Cremers FPM & Kremer H (2003) A mutation in the gamma actin 1 (ACTG1) gene causes autosomal dominant hearing loss (DFNA20/26). *J Med Genet* 40: 879–884

Wioland H, Guichard B, Senju Y, Myram S, Lappalainen P, Jégou A & Romet-Lemonne G (2017) ADF/Cofilin Accelerates Actin Dynamics by Severing Filaments and Promoting Their Depolymerization at Both Ends. *Curr Biol* 27: 1956-1967.e7

Wioland H, Jegou A & Romet-Lemonne G (2019) Quantitative Variations with pH of Actin Depolymerizing Factor/Cofilin's Multiple Actions on Actin Filaments. *Biochemistry* 58

Witjes L, Van Troys M, Verhasselt B & Ampe C (2020) Prevalence of cytoplasmic actin mutations in diffuse large B-cell lymphoma and multiple myeloma: A functional assessment based on actin three-dimensional structures. *Int J Mol Sci*

Yuan Y, Gao X, Huang B, Lu J, Wang G, Lin X, Qu Y & Dai P (2016) Phenotypic Heterogeneity in a DFNA20/26 family segregating a novel ACTG1 mutation. *BMC Genet*

Zhang F, Saha S, Shabalina SA & Kashina A (2010) Differential arginylation of actin isoforms is regulated by coding sequence-dependent degradation. *Science* 329: 1534–1537

Zimmet A, Van Eeuwen T, Boczkowska M, Rebowski G, Murakami K & Dominguez R (2020) Cryo-EM structure of NPF-bound human Arp2/3 complex and activation mechanism. *Sci Adv* 6: eaaz7651

1226 **Table 1 Comparison of biochemical parameters, velocities, rate and equilibrium constants**
1227 **measured in experiments with human cytoskeletal γ–actin and variant p.E334Q.**

1228

Parameter	γ–actin	p.E334Q	1:1 Mixture
IC_{50} [nM] (DNase–Inhibition)	22.7 ± 0.7	25.7 ± 0.6 **(* 1.1–fold ↑)**	–
T_M [°C] (Mg^{2+}–ATP–G–actin)	56.77 ± 0.24	56.19 ± 0.30 **(ns)**	–
T_M [°C] (Mg^{2+}–ADP–F–actin)	65.00 ± 0.76	64.83 ± 0.25 **(ns)**	–
k_{-T} [s^{-1}] (Mg^{2+}–ε–ATP)	0.0473 ± 0.0013	0.0972 ± 0.0019 **(**** 2.1–fold ↑)**	–
k_{-D} [s^{-1}] (Mg^{2+}–ε–ADP)	0.2155 ± 0.0017	0.3199 ± 0.0027 **(**** 1.5–fold ↑)**	–
F–actin ATPase [s^{-1}]	0.00089 ± 0.00005	0.00088 ± 0.00004 **(ns)**	–
k_{obs} [s^{-1}] bulk–polymerization rate (Δpyr-fluorescence)	0.0140 ± 0.0004	0.0129 ± 0.0008 **(*** 1.1–fold ↓)**	0.0134 ± 0.0006 **(* 1.04–fold ↓)**
k_{obs} [s^{-1}] + 10 nM Arp2/3 bulk–polymerization rate (Δpyr-fluorescence)	0.6441 ± 0.0163	0.5458 ± 0.02256 **(** 1.2–fold ↓)**	0.6162 ± 0.0776 **(ns)**
r_{obs}[nm s^{-1}] rate of filament elongation (TIRF–M)	12.6 ± 0.3	11.1 ± 0.3 **(**** 1.1–fold ↓)**	–
k_{obs} [s^{-1}] rate of filament disassembly (Δpyr-fluorescence)	0.0022 ± 0.0002	0.0029 ± 0.0003 **(**** 1.3–fold ↑)**	0.0023 ± 0.0002 **(ns)**
k_c [nM^{-1} s^{-1}] + cofilin rate of filament disassembly (Δpyr-fluorescence)	$3.42 \times 10^{-4} \pm 0.22 \times 10^{-4}$	$0.81 \times 10^{-4} \pm 0.08 \times 10^{-4}$ **(**** 4.2–fold ↓)**	$1.54 \times 10^{-4} \pm 0.11 \times 10^{-4}$ **(*** 2.2–fold ↓)**
v [nm s^{-1}] sliding velocity on NM2A–HMM	195.3 ± 5.0	39.1 ± 3.2 **(**** 5.0–fold ↓)**	131.2 ± 10.0 **(*** 1.5–fold ↓)**
v [nm s^{-1}] sliding velocity on Myo5A–HMM at optimal myosin density	315.1 ± 28.9	190.4 ± 46.9 **(**** 1.7–fold ↓)**	–
K_{app} [μM] (NM2A–HMM)	3.20 ± 0.74	2.89 ± 0.49 **(ns)**	–
k_{cat} [s^{-1}] (NM2A-HMM)	0.097 ± 0.002	0.076 ± 0.005 **(* 1.3–fold ↓)**	–
k_{-A} [s^{-1}] (NM2A–2R)	$8.0\times10^{-5} \pm 3.3 \times10^{-6}$	$4.5\times10^{-4} \pm 6.7\times10^{-6}$ **(**** 5.6–fold ↑)**	$2.3\times10^{-4} \pm 1.3\times10^{-5}$ **(*** 2.9–fold ↑)**
k_{-A} [s^{-1}] (NM2C-2R)	$3.1\times10^{-4} \pm 5.0\times10^{-6}$	$1.7\times10^{-3} \pm 5.8\times10^{-5}$ **(*** 5.6–fold ↑)**	$6.7\times10^{-4} \pm 1.5\times10^{-5}$ **(*** 2.2–fold ↑)**
K_A [nM] (NM2A–2R)	1.7 ± 0.3	16.9 ± 0.3 **(** 9.9–fold ↑)**	–
K_{DA} [nM] (NM2A–2R)	122.6 ± 11.4	353.0 ± 20.6 **(** 2.9–fold ↑)**	–
Coupling (K_{DA}/ K_A) (NM2A-2R)	72.1	20.9 **(**** 3.5–fold ↓)**	–
$1/K_1$ [μM] (NM2A–2R)	812.1 ± 82.7	863.8 ± 91.6 **(ns)**	–

k_{+2} [s^{-1}] (NM2A–2R)	461.7 ± 18.6	435.6 ± 16.5 **(ns)**	–
K_1k_{+2} [μM^{-1} s^{-1}] (NM2A–2R)	0.276 ± 0.002	0.272 ± 0.005 (ns)	–

1229
1230

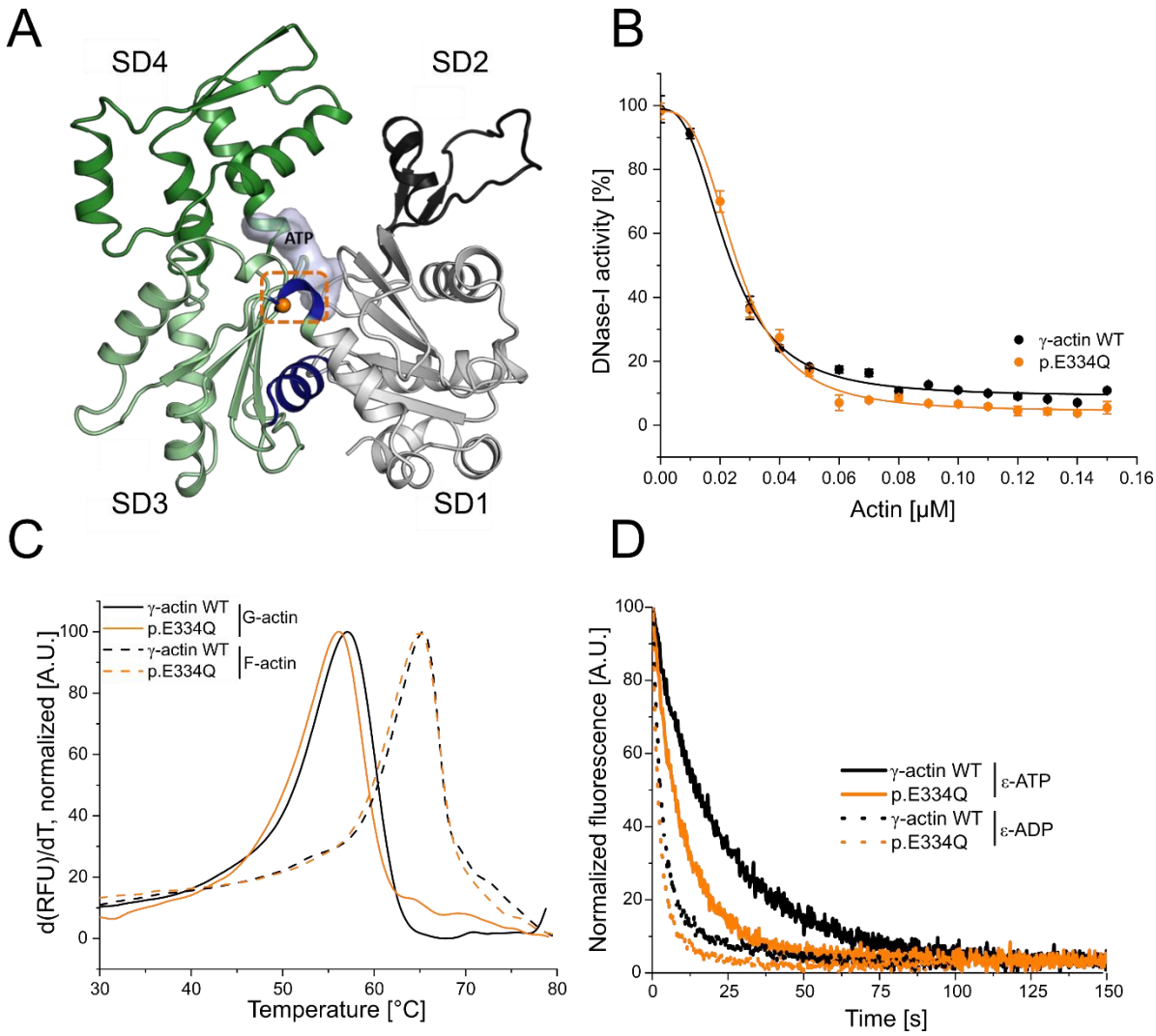

Figure 1. Analysis of actin folding, thermal stability and nucleotide exchange (A) Homology model of human cytoskeletal γ–actin (based on PDB–ID: 2BTF). Subdomains (SDs) of actin are colored in grey (SD1), dark grey (SD2), light green (SD3) and green (SD4). The hinge region encompassing residues 137–145 and 333–338 is colored in blue. The mutant residue E334 is shown as an orange sphere. **(B)** Inhibition of DNase–I activity by monomeric γ–actin WT and p.E334Q. Data is the mean of three individual experiments ± SD. A Hill equation was fitted to the data, which yields the half–maximal inhibitory concentration (IC_{50}, Table 1). **(C)** The protein denaturation temperature of monomeric and filamentous p.E334Q and WT actin were determined by DSF. Representative experimental traces are shown. The protein denaturation temperature is derived from the peak of the melting curve (Table 1) (p.E334Q (G-actin), N=3; WT (G-actin), N=5; p.E334Q (F–actin), N=5; WT (F–actin), N=5). **(D)** Nucleotide exchange rates (k_{-T}, k_{-D}) were determined for monomeric p.E334Q and γ–actin WT using fluorescently labeled ATP (ε–ATP) (p.E334Q, N=18; WT, N=21) and ADP (ε–ADP) (p.E334Q, N=11; WT, N=11) Representative experimental traces are shown. Rates were determined by fitting a single exponential function to the data (Table 1).

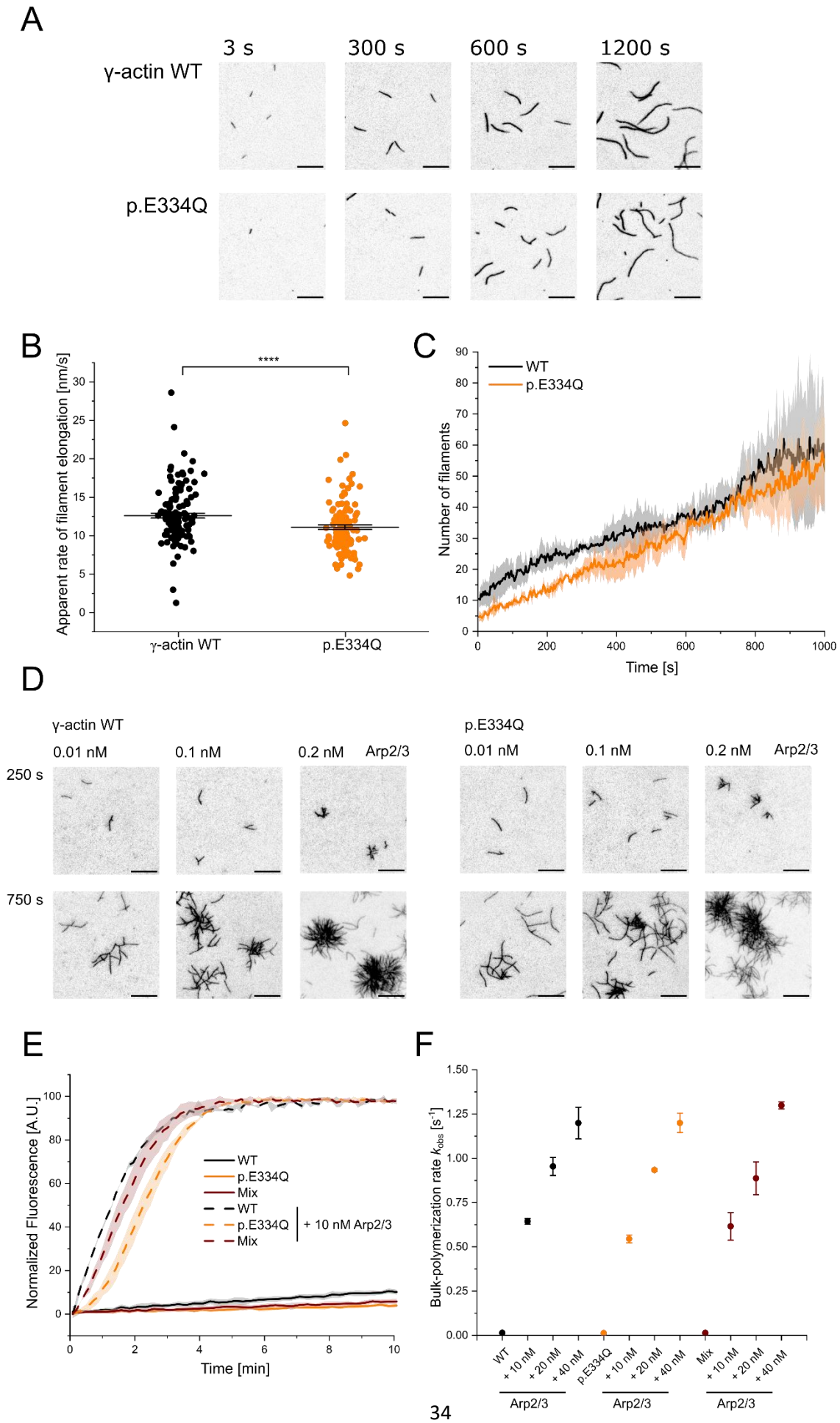
A
3 s
300 s
600 s
1200 s
γ-actin WT
p.E334Q
B
Apparent rate of filament elongation [nm/s]
****
γ-actin WT
p.E334Q
C
WT
p.E334Q
Number of filaments
Time [s]
D
γ-actin WT
p.E334Q
0.01 nM
0.1 nM
0.2 nM
Arp2/3
250 s
750 s
E
Normalized Fluorescence [A.U.]
WT
p.E334Q
Mix
+ 10 nM Arp2/3
Time [min]
F
Bulk-polymerization rate k_{obs} [s^{-1}]
WT
p.E334Q
Mix
+ 10 nM
+ 20 nM
+ 40 nM
Arp2/3

1247

1248 **Figure 2. Analysis of the polymerization capacity of WT and p.E334Q γ–actin in the absence and**
1249 **presence of human Arp2/3 complex. (A)** Polymerization of p.E334Q and WT γ–actin (1 µM, 10% Atto–
1250 655 labeled) was induced by salt–shift and the progression of the reaction was tracked by TIRF
1251 microscopy. Shown are representative micrographs at the indicated points in time. Scale bar
1252 corresponds to 10 µm. **(B)** The elongation rates of individual filaments were determined by manual
1253 tracking of the elongating barbed ends of the filaments. Every data point represents an individual
1254 filament (WT: n = 128 filaments, p.E334Q: n = 114 filaments). Data is shown as the mean ± SEM. **(C)**
1255 Nucleation efficiencies were determined by monitoring changes in the number of filaments over the
1256 time of the polymerization experiments. The solid lines and shades represent the mean ± SD of four
1257 individual experiments. **(D)** TIRF microscopy–based observation of human Arp2/3 complex mediated
1258 differences in the salt-induced polymerization of p.E334Q and WT γ–actin (1 µM, 10% Atto–655
1259 labeled). Shown are representative micrographs at the indicated points in time. For both WT and
1260 p.E334Q γ–actin, the formation of the first branch points was observed after 250 s in the presence of
1261 0.01 nM Arp2/3. Scale bar corresponds to 10 µm. N=3 for each Arp2/3 concentration **(E)** Pyrene–based
1262 polymerization experiment of 2 µM γ–actin WT, p.E334Q actin, or a 1:1 mixture of both (5% pyrene–
1263 labeled) in the absence and presence of Arp2/3. Shown are representative traces. The solid
1264 lines/shades represent the mean ± SD of at least three individual experiments. **(F)** Bulk–polymerization
1265 rates determined from the experiments shown in (E). Data is shown as the mean ± SD of all performed
1266 experiments. N=3 for each Arp2/3 concentration. N=12 for all experiments performed in the absence
1267 of Arp2/3. Individual k_{obs} values and differences with statistical significance are summarized in Table 1.

1268

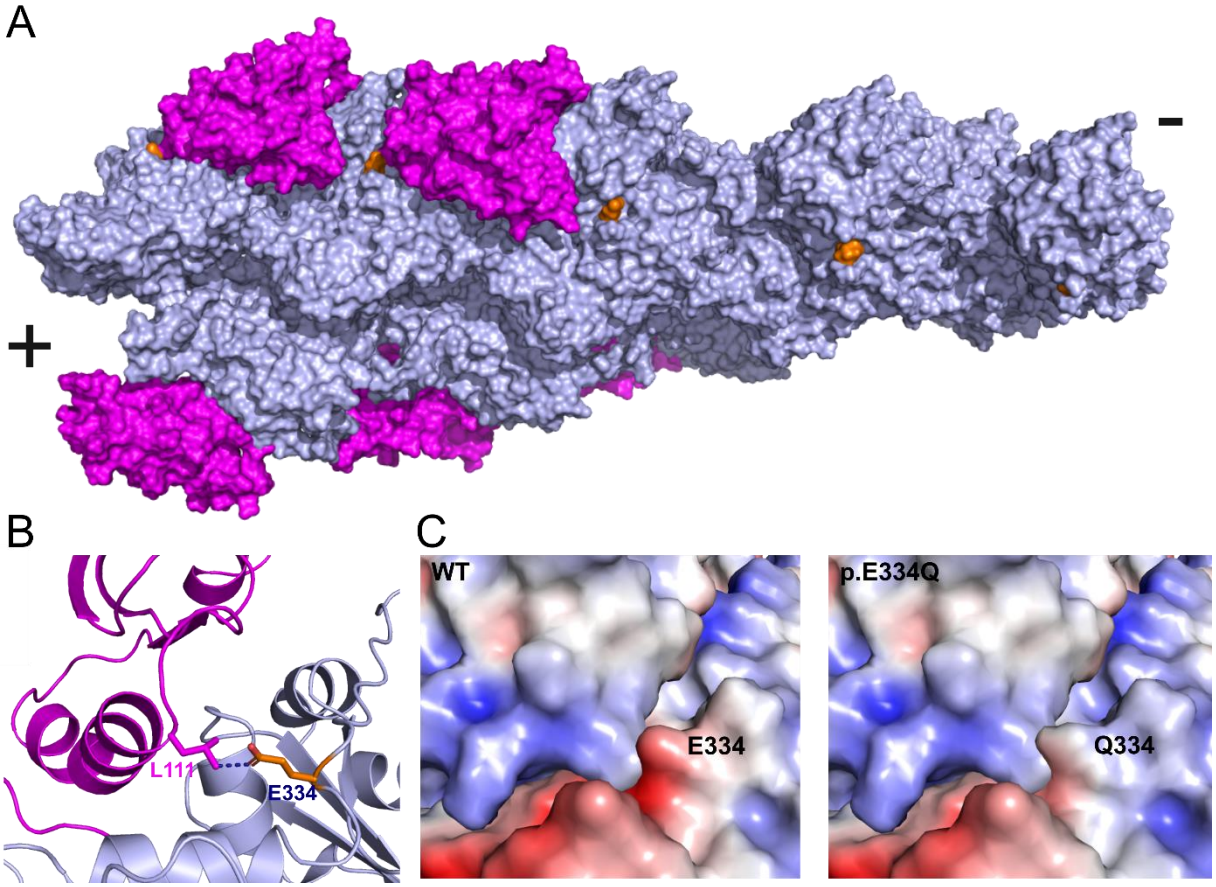

Figure 3. *In silico* analysis of the effects of the E334Q mutation on the actin–cofilin interaction. (A) Human homology model of a cytoskeletal γ–actin filament partially decorated with cofilin–1 (model based on PDB–ID: 6UC4). Cofilin–1 is colored magenta, actin monomers are depicted in light blue and the actin residue E334 is colored orange. **(B)** Close up showing the details of the Van der Waals interaction between E334 and cofilin residue L111 on the pointed end side. The length of the dotted line between the side chains of actin-E334 and cofilin-L111 corresponds to 3.1 Å in our model. **(C)** The change in surface charge at the actin-cofilin interaction interface introduced by mutation E334Q is visualized by coulombic surface coloring.

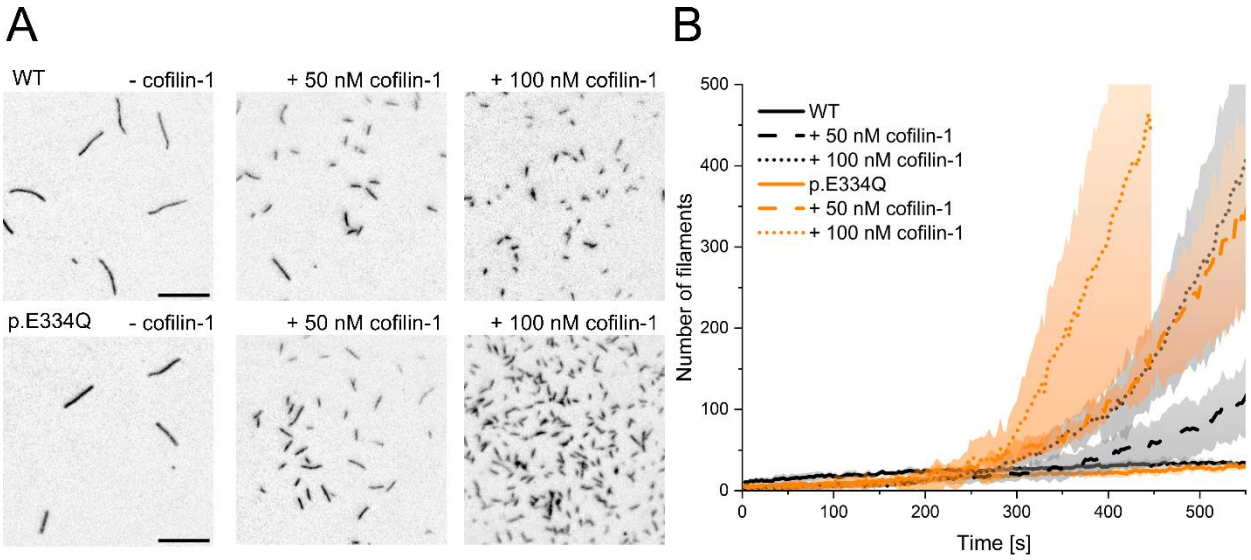

1282 **Figure 4. Analysis of the effect of cofilin–1 on the spontaneous polymerization of WT and p.E334Q**
1283 **γ–actin. (A)** TIRF microscopy–based observation of cofilin–1 mediated differences in the salt-induced
1284 polymerization of p.E334Q and WT γ–actin (1 µM, 10% Atto–655 labeled). Shown are representative
1285 micrographs 450 s after induction of polymerization. Scale bar corresponds to 10 µm. **(B)** Time
1286 dependence of the increase in filaments observed by TIRF microscopy. The solid and dotted lines and
1287 shades represent the mean ± SD of 3 individual experiments.

1288

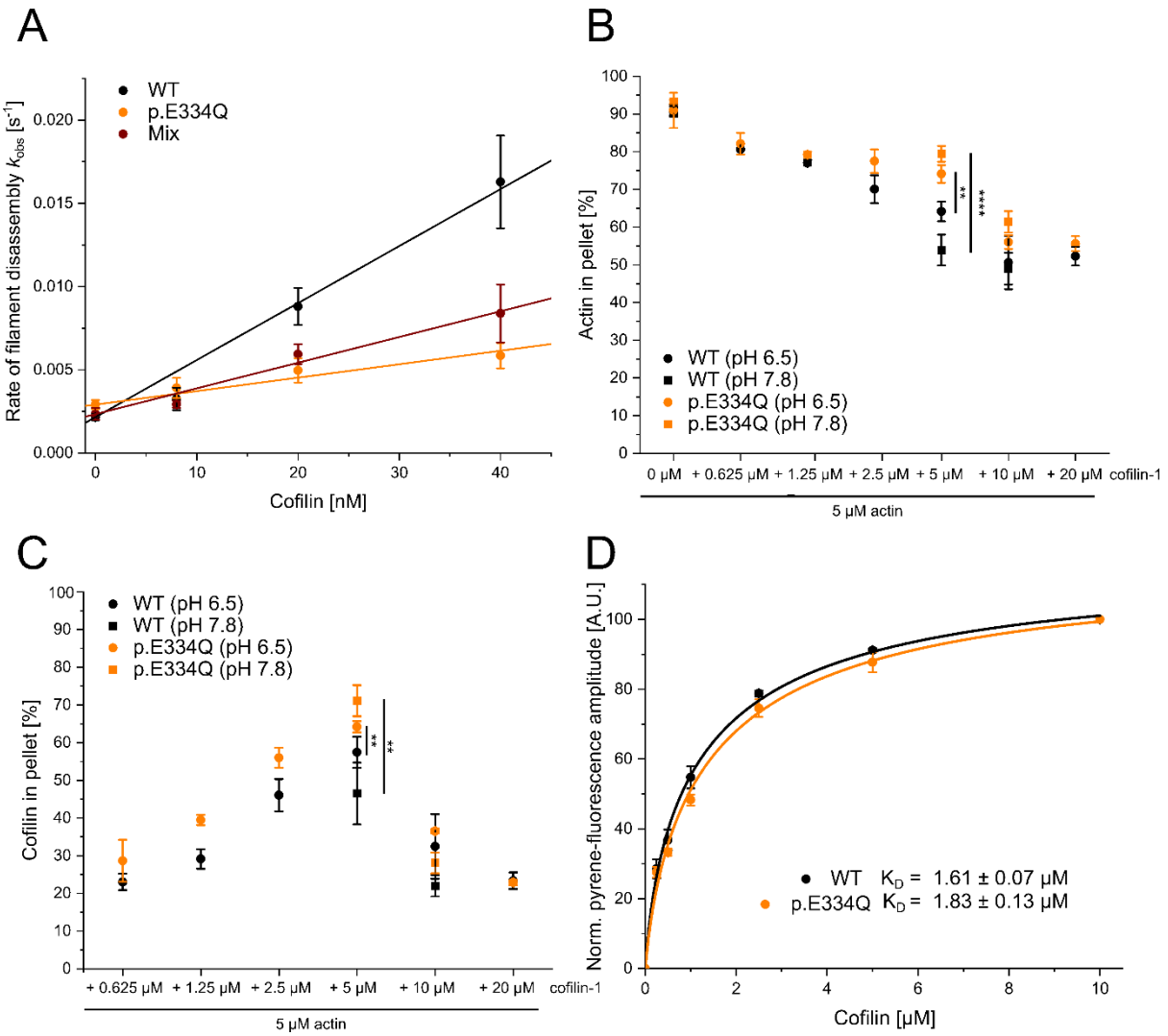

Figure 5. Analysis of the interaction of filamentous WT and p.E334Q γ–actin with cofilin–1. (A) Pyrene-based dilution–induced depolymerization experiments (5 % pyrene–labeled actin) were used to quantify the impact of cofilin–1 on the disassembly of filaments formed by p.E334Q, WT and a 1:1 mixture of p.E334Q and WT γ–actin. Depolymerization was induced by adding G–buffer (pH 7.8). Representative experimental traces showing the decrease in pyrenyl fluorescence over time are given in **Figure 5 – figure supplement 1**. The observed values of the rate constants show a linear dependence on the cofilin-1 concentration in the range of 0-40 nM, with the slopes corresponding to the apparent second-order rate constant (k_C) for cofilin–1–induced depolymerization. Values for k_C are summarized in Table 1. Data is shown as the mean ± SD of 8–14 individual experiments. **(B, C)** In addition, cofilin–1 binding to actin filaments and cofilin-1 mediated filament disassembly at different pH values (pH 6.5, pH 7.8) was investigated in co–sedimentation experiments. The data are given as mean ± SD. N=6 for experiments performed at pH 7.8. N=7 for experiments performed at pH 6.5 in the absence of cofilin. N=3 for experiments performed at pH 6.5 in the presence of cofilin. **(D)** The dissociation equilibrium constant (K_D) for binding of cofilin–1 to pyrene-labeled WT or p.E334Q filaments was determined by monitoring the change in fluorescence amplitude upon cofilin-1 binding. Data is shown as the mean ± SD. N=8 for WT, N=9 for p.E334Q.

1308

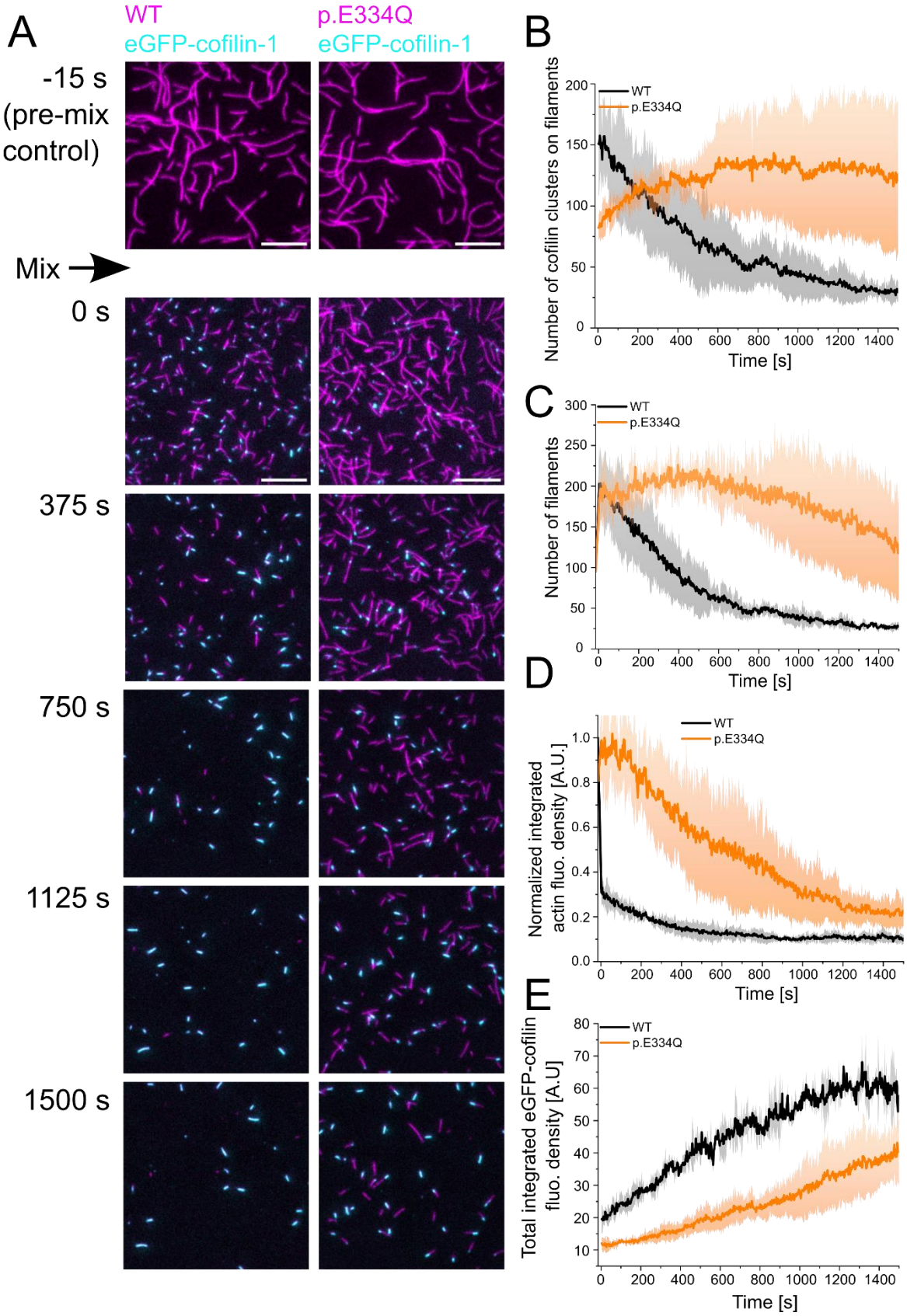

1309

1310 **Figure 6. Analysis of the interaction of WT and p.E334Q γ–actin with eGFP–cofilin–1 (A)** The
1311 disassembly of 300 nM "aged" WT and p.E334Q F–actin (10% Atto–655 labeled, capped by CP) in the
1312 presence of 100 nM eGFP–cofilin–1 was visualized using two–color TIRF microscopy. F–actin is shown
1313 in magenta, eGFP–cofilin in cyan. Shown are representative micrographs at the indicated time points.

1314 Scale bar corresponds to 10 µm. **(B)** Time dependence of the change in the number of eGFP–cofilin–1
1315 clusters on actin filaments. The solid lines and shades represent the mean ± SD of three individual
1316 experiments. **(C)** Time dependence of the decrease in filament count. The solid lines and shades
1317 represent the mean ± SD of three individual experiments. **(D)** Temporal tracking of actin filament
1318 disassembly by monitoring changes in total actin fluorescence per image frame. The solid lines and
1319 shades represent the mean ± SD of three individual experiments. **(E)** Visualization of temporal changes
1320 in the abundance of eGFP–cofilin–1 clusters based on monitoring total eGFP–cofilin–1 fluorescence
1321 per image frame. The solid lines and shades represent the mean ± SD of three individual experiments.

1322

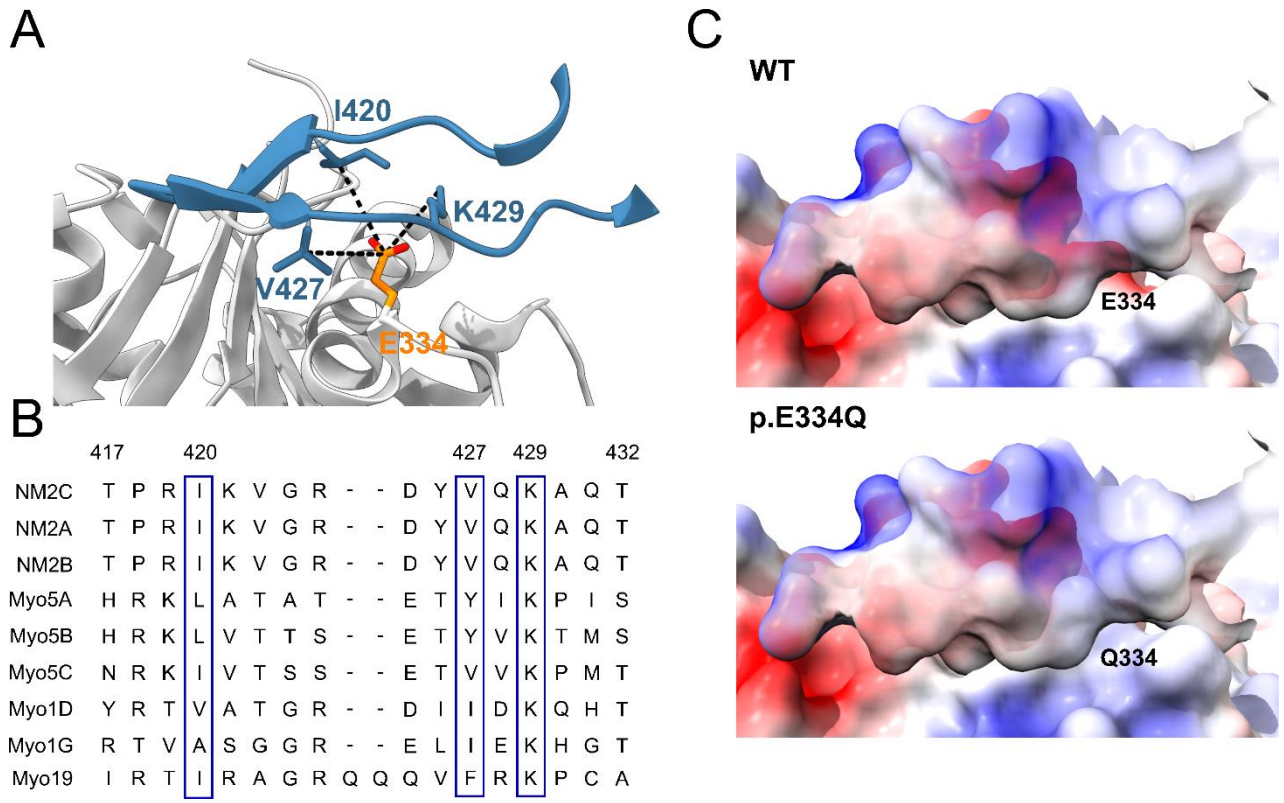

Figure 7. *In silico* analysis of the effects of the E334Q mutation on the actin–myosin interaction. (A) Contact region between the CM–loop of NM2C (blue) and residue E334 (orange) in cytoskeletal γ–actin (PDB–ID: 5JLH) (Von Der Ecken *et al*, 2016). Actin interacts with a core contact triad in the myosin CM-loop, which in the case of NM2C consists of lysine K429 and hydrophobic residues I420 and V427. **(B)** Multiple sequence alignment of the CM-loop of selected cytoskeletal myosin isoforms. The alignment shows complete sequence identity for NM2C, NM2A and conservation of residues contributing to the core contact triad in class 5, class 19 and selected members of class 1 myosins (blue boxes). Residue numbering refers to the NM2C primary structure. **(C)** Mutation E334Q leads to a weakening of complementary electrostatic interactions. The interaction interface involving the CM-loop of NM2C and the region affected by the mutation on cytoskeletal γ–actin is visualized by coulombic surface coloring. Positive potentials are shown in blue, and negative potentials in red.

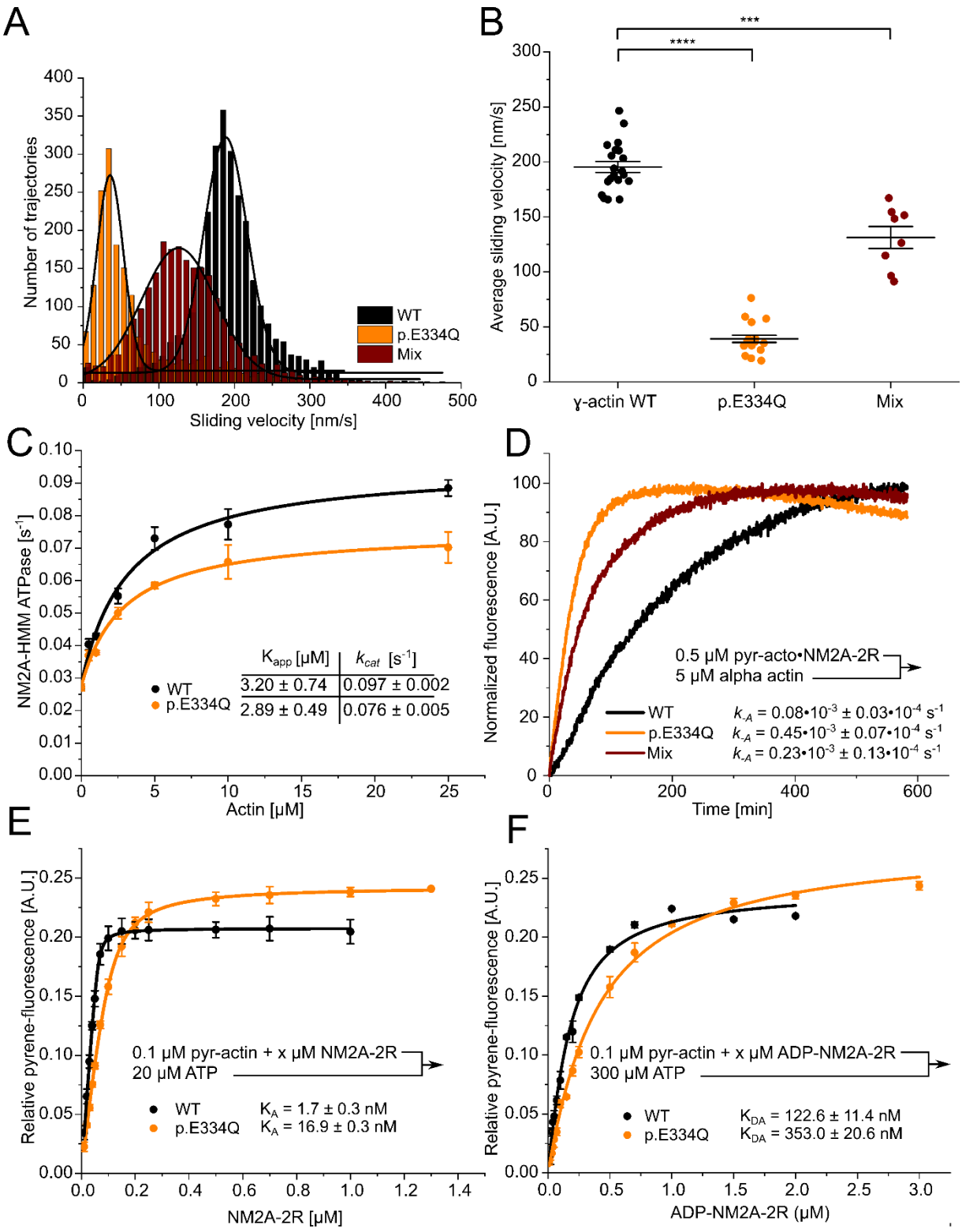

Figure 8. Analysis of the interaction of human NM2A with WT and p.E334Q γ–actin. (A) The interaction of surface–immobilized NM2A–HMM with WT γ–actin filaments, p.E334Q γ–actin filaments and heterofilaments (1:1 mixture) was analyzed using the unloaded *in vitro* motility assay. Representative velocity distributions are obtained from recorded trajectories of WT and mutant filaments in a single experiment. The average sliding velocity of the filaments in each experiment was determined by applying a Gaussian fit (black line) to the obtained velocity distributions. (**B**) Secondary plot of all measured sliding velocities. Each data point represents a single experiment (N=20 for WT

1344 filaments, N=18 for p.E334Q filaments, N=8 for heterofilaments) in which the sliding velocities of a
1345 minimum of 600 filaments have been analyzed. The average sliding velocity in each experiment was
1346 determined as described in (A). Data is shown as the mean ± SEM. **(C)** The ability of p.E334Q and WT
1347 filaments to activate the NM2A–HMM ATPase was analyzed using a NADH–coupled enzymatic assay.
1348 The data is best described by a hyperbolic fit that yields K_{app} (apparent K_m for actin) and k_{cat} (maximal
1349 turnover). Data is shown as the mean ± SD of three individual experiments. **(D)** Determination of the
1350 dissociation rate constant (k_{-A}) for the interaction of NM2A–2R with p.E334Q or WT γ–actin in the
1351 absence of nucleotide. k_{-A} was determined in displacement experiments by chasing pyrene–labeled
1352 acto•NM2C-2R with a large excess of unlabeled F-actin. Shown are representative traces. The shown
1353 k_{-A} values are the results of 5–11 individual experiments. Data were fitted using a single exponential
1354 function. **(E, F)** The affinity of WT and p.E334Q γ–actin for NM2A–2R in the absence (K_A) and in the
1355 presence of saturating ADP concentrations (K_{DA}) was determined using the method developed by
1356 Kurzawa and Geeves (Kurzawa & Geeves, 1996). Increasing concentrations of myosin were dissociated
1357 from pyrene–labeled WT or p.E334Q F–actin by mixing the complex with excess ATP. The obtained
1358 fluorescence amplitudes of the individual transients were plotted against the corresponding myosin
1359 concentrations. A quadratic equation (see Material and Methods) was fitted to the data, which yields
1360 the respective affinity. Data is shown as the mean ± SD of three individual experiments.

1361

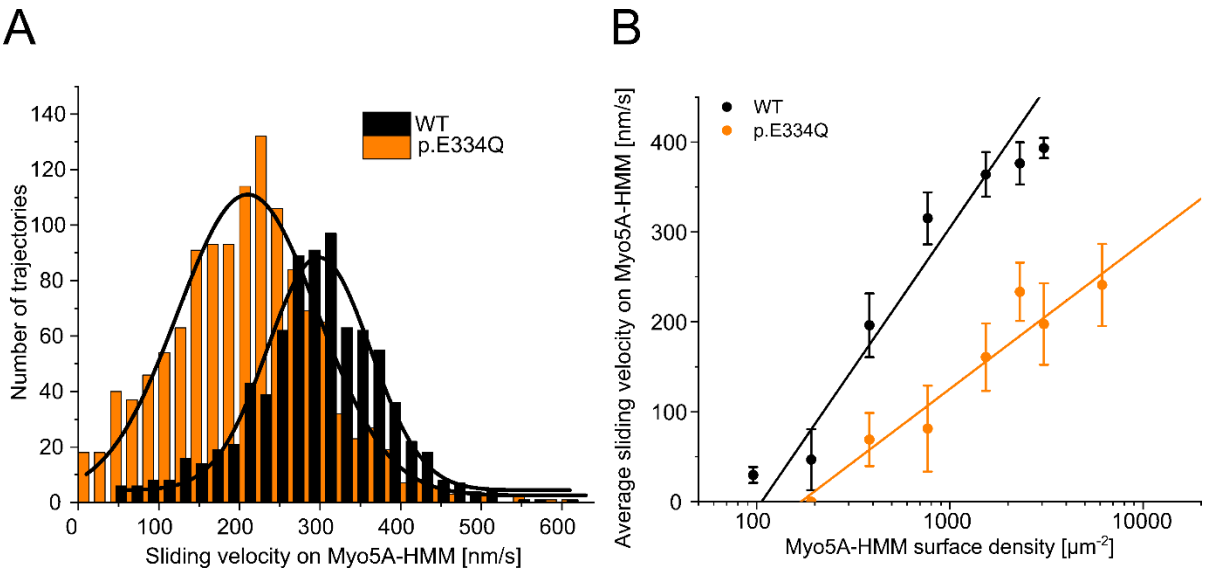

Figure 9 Analysis of the interaction of human Myo5A-HMM with WT and p.E334Q γ–actin in the unloaded *in vitro* motility assay at different Myo5A surface densities. (A) The interaction of surface–immobilized Myo5A–HMM with WT γ–actin and p.E334Q γ–actin filaments was analyzed using the unloaded *in vitro* motility assay. Representative velocity distributions were obtained from one individual experiment at the optimal Myo5A-HMM surface density for WT (770 μm^{-2}) and p.E334Q filaments (3100 μm^{-2}). The average sliding velocity of the filaments in each experiment was determined by applying a Gaussian fit (black line) to the obtained velocity distributions. **(B)** Semi–logarithmic plot summarizing all measured sliding velocities at different Myo5A–HMM surface densities. Data is shown as the mean ± SD of 3–10 individual experiments. The dependence of the average sliding velocity on surface motor density is best–described in the semi–logarithmic graph by lines up to approximately 1000 motors μm^{-2} for WT filaments and 7000 motors μm^{-2} for p.E334Q filaments.

1374 Supplementary Figures

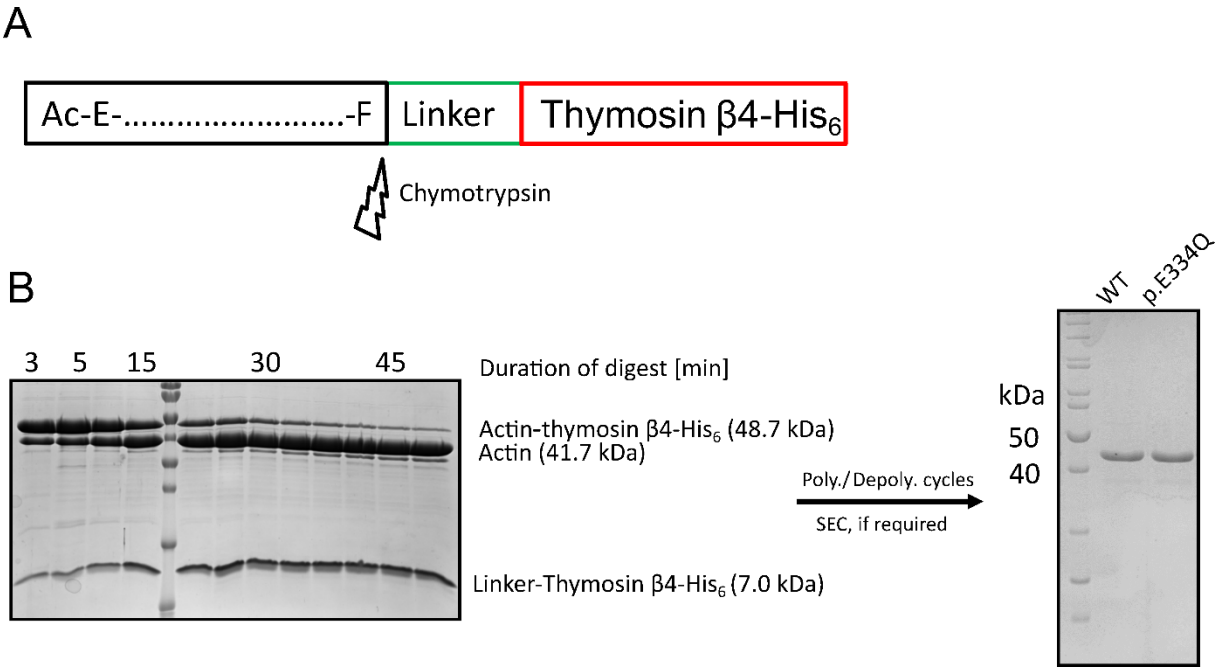

1375

1376 **Figure 1 – figure supplement 1.** Purification of recombinant WT and p.E334Q γ–actin from *Spodoptera*
1377 *frugiperda* (Sf–9). **(A)** Recombinant WT and p.E334Q γ–actin were produced in the form of actin–
1378 thymosin β4–His_6 fusion proteins. The C-terminal linker and tag sequence are removed by
1379 chymotrypsin-mediated cleavage after the C-terminal residue of the native γ–actin sequence (Phe). **(B)**
1380 Exemplary polyacrylamide gels from different stages of the purification. Left gel: The actin– thymosin
1381 β4–His_6 fusion protein is digested by treatment with chymotrypsin. The digest is stopped by treatment
1382 with PMSF. Time of digest strongly depends on the age and the batch of chymotrypsin and was
1383 determined by multiple test digests for each actin preparation. For the preparation pictured here, the
1384 fusion protein was digested for 50 min with a (w/w) ratio of 1:300 (chymotrypsin:actin). Molecular
1385 weight marker: PageRuler Prestained (Thermo Fisher Scientific, Waltham, MA, USA). Right gel: After
1386 the digest was stopped, the actin was subjected to polymerization/depolymerization cycles and, if
1387 necessary, size exclusion chromatography to obtain the final product. Molecular weight marker:
1388 PageRuler Unstained (Thermo Fisher Scientific, Waltham, MA, USA).

1389

1390

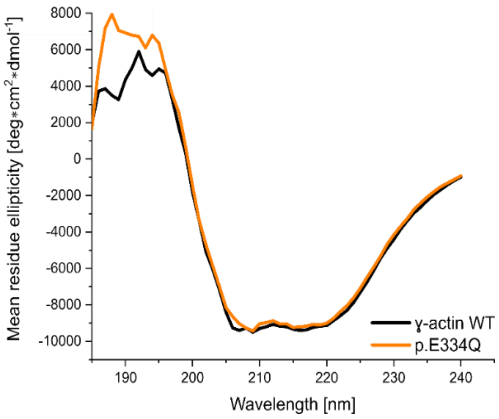

	α–helix	β–strand	Turns	Unordered	Total
γ–actin WT	22 %	24 %	22 %	31 %	99 %
p.E334Q	21 %	26 %	22 %	31 %	100 %

1391

1392 **Figure 1 – figure supplement 2.** CD–Spectra of γ–actin WT and p.E334Q protein. Shown are the
1393 smoothed (Savitsky–Golay) and averaged spectra with the averaged buffer spectrum subtracted. The
1394 depicted secondary structure composition of γ–actin WT and p.E334Q protein was determined by using
1395 the DichroWeb online platform.

1396

1397

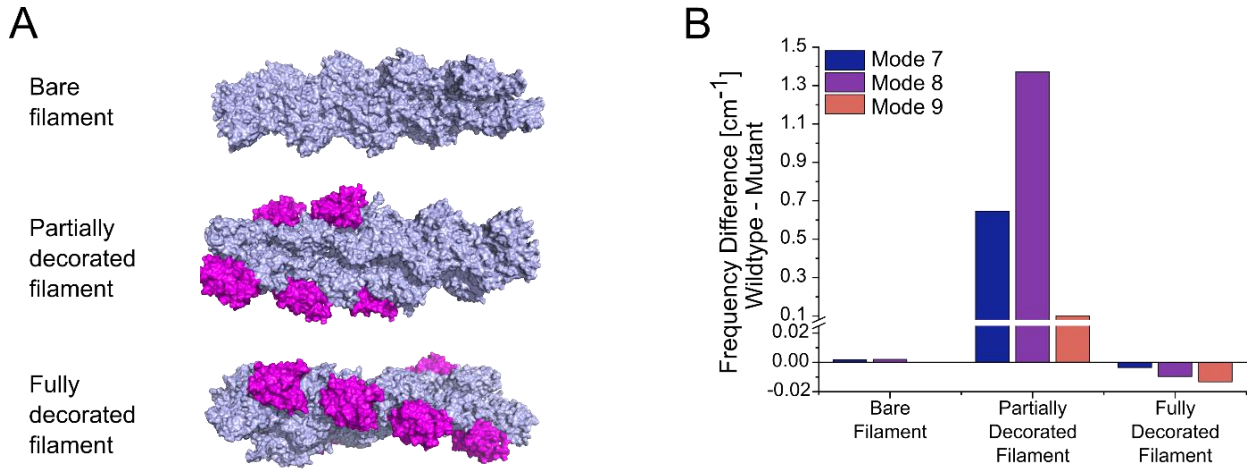

1398

1399 **Figure 3 – figure supplement 1. Normal mode analysis of changes induced by mutation E334Q in the**
1400 **global mobility of bare, partially and a fully cofilin-1 decorated γ–actin mini-filaments (A)** Models of
1401 a bare γ–actin mini-filament, a partially and a fully cofilin-1 decorated γ–actin mini-filament were
1402 generated for normal mode analysis. Each mini–filament consists of nine actin monomers. Actin is
1403 colored light blue and cofilin–1 magenta. **(B)** Significant differences in the global mobility of the
1404 different types of mini–filaments shown in panel (A), containing either WT or mutant cytoskeletal γ–
1405 actin, were only observed in the case of partial cofilin-1 decoration. Large differences are observed for
1406 partially decorated filaments in modes 7, 8 and 9, which are the global motions with the lowest
1407 frequencies.

1408

1409

1410

1411

1412

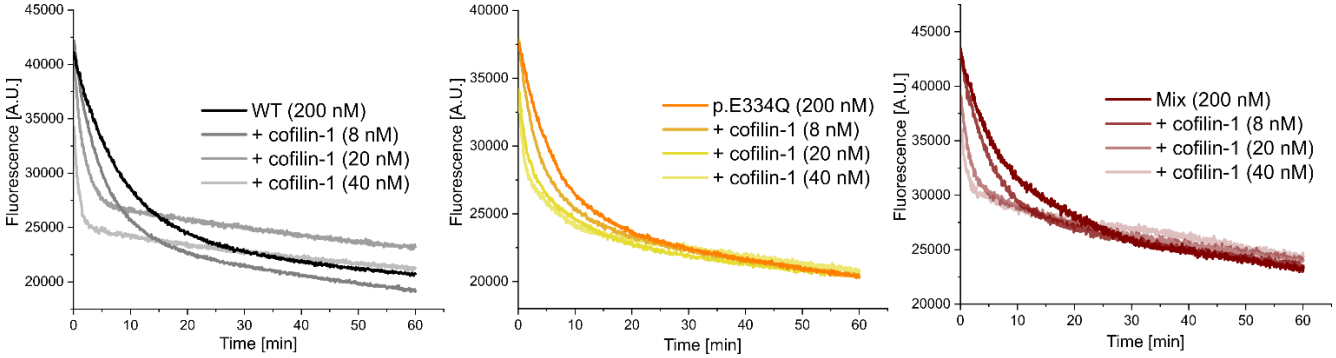

1413 **Figure 5 – figure supplement 1.** Exemplary traces of dilution–induced depolymerization experiments
1414 in the absence and presence of increasing concentrations of human cofilin–1**.**

1415

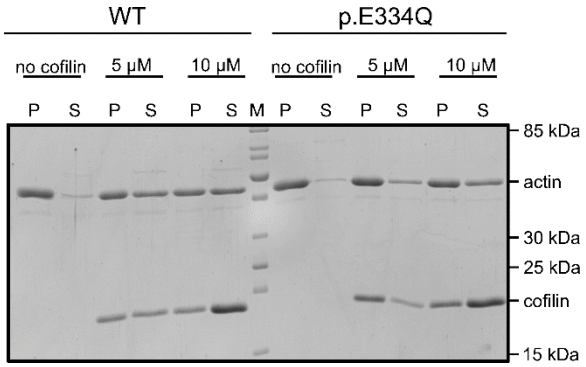

1416

1417 **Figure 5 – figure supplement 2.** Exemplary polyacrylamide gel showing a co–sedimentation
1418 experiment performed with 5 µM WT and p.E334Q γ–actin in the absence and presence of 5 µM or 10
1419 µM cofilin-1 at pH 7.8.

1420

1421

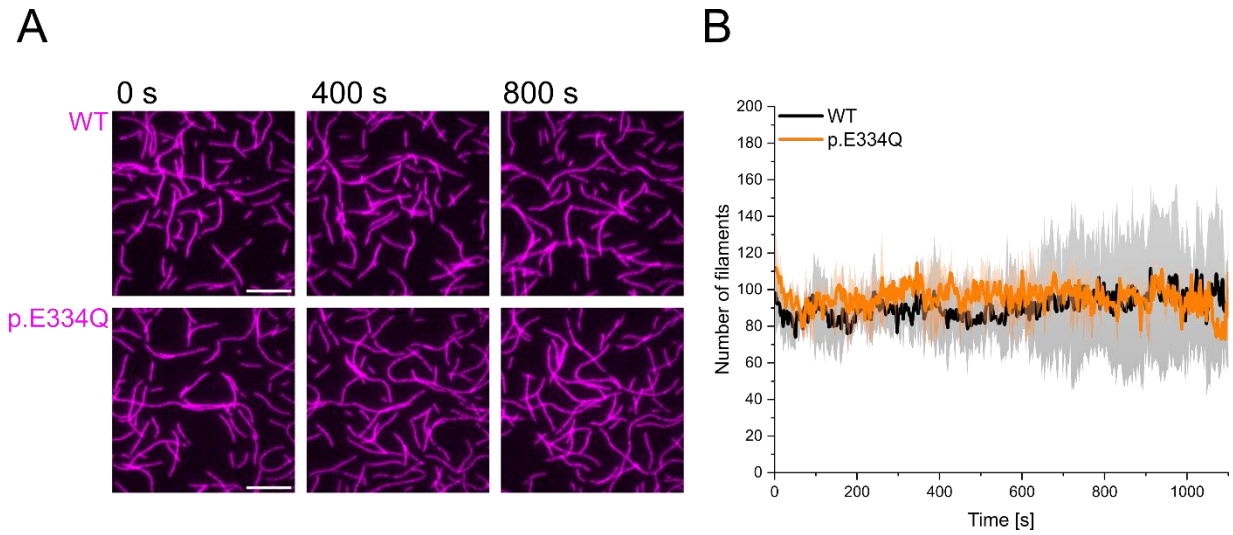

Figure 6 – figure supplement 1. Control experiments showing that E334Q and WT γ–actin filaments are stable over a period of 1000 s. (A) 300 nM "aged" WT and p.E334Q F–actin (10% Atto–655 labeled, capped by CP) was visualized using TIRF microscopy. Shown are representative micrographs at the indicated time points. Scale bar corresponds to 10 µm. **(B)** Quantification of the number of actin filaments over the time of the experiment. The solid lines and shades represent the mean ± SD of 2–3 individual experiments.

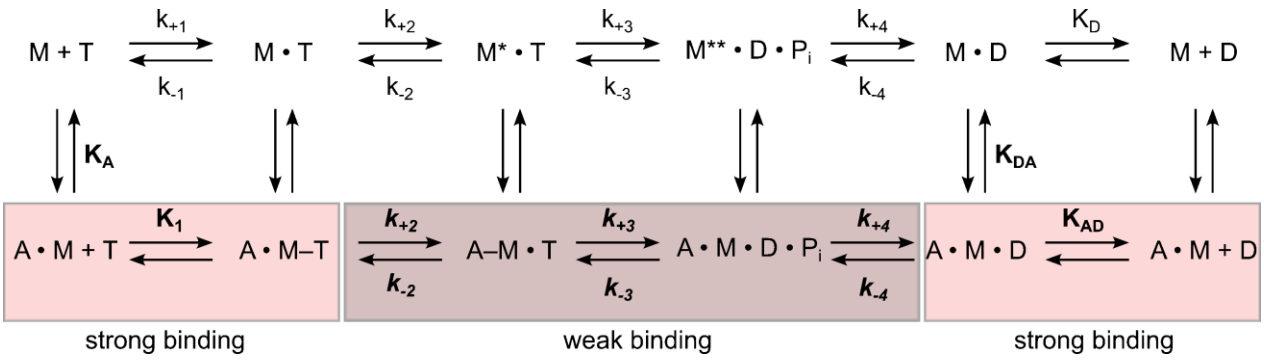

Figure 8 – figure supplement 1. Schematic representation of the basic reaction pathway of myosin- and actomyosin catalyzed ATP hydrolysis and ATP conversion. The notation for the description of the kinetic parameters shows rate constants in italics and equilibrium constants in normal type; the notation distinguishes between the constants in the presence and absence of F-actin by using boldface ($\boldsymbol{k_{+1}}$ and $\mathbf{K_1}$) versus normal type (k_{+1} and K_1); subscripts A and D refer to actin ($\mathbf{K_A}$) and ADP (K_D), respectively. $\mathbf{K_A}$ represents the affinity of myosin for F-actin, K_D the affinity of ADP for myosin, $\mathbf{K_{AD}}$ the affinity of ADP for the actomyosin complex, and K_{DA} the affinity of actin for myosin in the presence of saturating [ADP]. M refers to myosin and P_i to inorganic phosphate. The asterisk represents different conformational states of the myosin motor domain.

1444

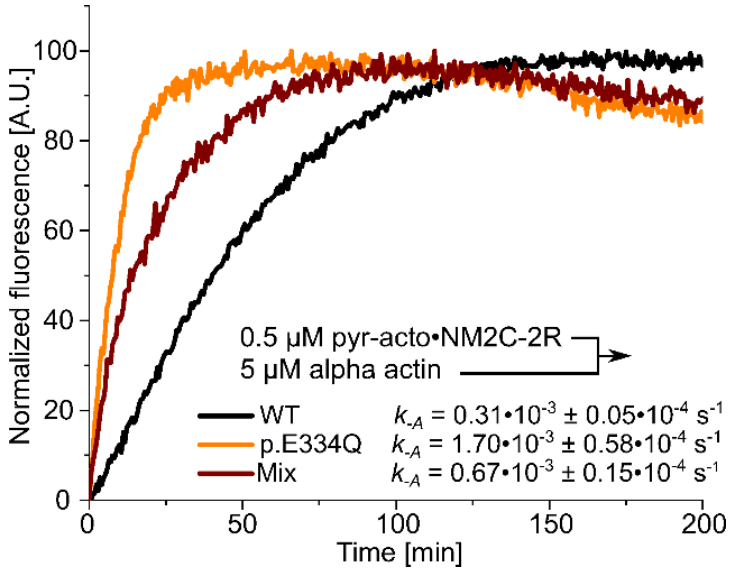

1445

1446 **Figure 8 – figure supplement 2. Determination of the dissociation rate constants (k_{-A}) for the**
1447 **interaction of NM2C-2R with p.E334Q or WT γ–actin in the absence of nucleotide.** Values for k_{-A} were
1448 directly measured by chasing pyrene–labeled acto-NM2C-2R with a large excess of unlabeled F-actin.
1449 Shown are representative traces. The k_{-A} values are the results of 5–11 individual experiments.

1450

1451

1452

1453

1454

1455

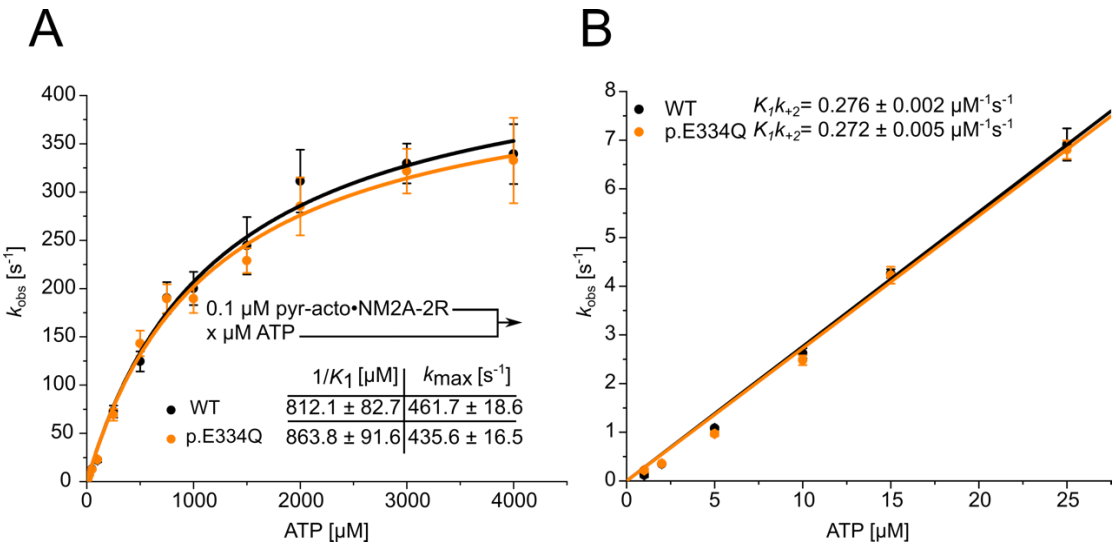

Figure 8 – figure supplement 3. Analysis of the apparent ATP–affinity (1/K_1), the maximal ATP–induced dissociation rate of NM2A from actin (k_{+2}) and the second-order rate constant for ATP binding (K_1k_{+2}) for complexes formed between NM2A-2R and WT or p.E334Q filaments. (A) ATP-induced dissociation experiments with phalloidin–stabilized pyrene–labeled acto–NM2A–2R complexes were performed as described in **Material and Methods.** A hyperbolic fit to the obtained data yields 1/K_1 and k_{+2}. Data is shown as the mean ± SD of six individual experiments. **(B)** A linear fit to the data obtained with low ATP concentrations (0 – 25 μM) yields K_1k_{+2}.